

An Improved Perturbation Pressure Closure for Eddy-Diffusivity Mass-Flux Schemes

Jia He^{1,1}, Yair Cohen^{1,1}, Ignacio Lopez-Gomez^{1,1}, Anna Jaruga^{2,2}, and Tapio Schneider^{1,1}

¹California Institute of Technology

²Caltech

November 30, 2022

Abstract

Convection parameterizations such as eddy-diffusivity mass-flux (EDMF) schemes require a consistent closure formulation for the perturbation pressure, which arises in the equations for vertical momentum and turbulence kinetic energy (TKE). Here we derive an expression for the perturbation pressure from approximate analytical solutions for 2D and 3D thermal bubbles. The new closure combines modified pressure drag and virtual mass effects with a new momentum advection damping term. This advection damping is an important source in the lower half of the thermal bubble and at cloud base levels in convective systems. It represents the effect of the perturbation pressure to ensure the non-divergent properties of the flow. The new formulation represents the pressure drag to be inversely proportional to updraft depth. This is found to significantly improve simulations of the diurnal cycle of deep convection, without compromising simulations of shallow convection. It is thus a key step toward a unified scheme for a range of convective motions. By assuming that the pressure only redistributes TKE between updrafts and the environment laterally, a closure for the velocity pressure-gradient correlation is obtained from the perturbation pressure closure. This novel pressure closure is implemented in an extended EDMF scheme and is shown to successfully simulate a rising bubble as well as shallow and deep convection in a single column model.

An Improved Perturbation Pressure Closure for Eddy-Diffusivity Mass-Flux Schemes

Jia He¹, Yair Cohen¹, Ignacio Lopez-Gomez¹, Anna Jaruga¹, Tapio
Schneider^{1,2}

¹California Institute of Technology, Pasadena, California, USA.

²Jet Propulsion Laboratory, California Institute of Technology, Pasadena, California, USA.

Key Points:

- An analytical closure for the perturbation pressure in convection parameterizations is derived.
- The closure combines the effects of virtual mass, momentum advection damping, and pressure drag.
- The closure performs well in simulating a rising bubble and the diurnal cycle of deep convection.

Corresponding author: Jia He, jiahe@caltech.edu

Abstract

Convection parameterizations such as eddy-diffusivity mass-flux (EDMF) schemes require a consistent closure formulation for the perturbation pressure, which arises in the equations for vertical momentum and turbulence kinetic energy (TKE). Here we derive an expression for the perturbation pressure from approximate analytical solutions for 2D and 3D thermal bubbles. The new closure combines modified pressure drag and virtual mass effects with a new momentum advection damping term. This advection damping is an important source in the lower half of the thermal bubble and at cloud base levels in convective systems. It represents the effect of the perturbation pressure to ensure the non-divergent properties of the flow. The new formulation represents the pressure drag to be inversely proportional to updraft depth. This is found to significantly improve simulations of the diurnal cycle of deep convection, without compromising simulations of shallow convection. It is thus a key step toward a unified scheme for a range of convective motions. By assuming that the pressure only redistributes TKE between updrafts and the environment laterally, a closure for the velocity pressure-gradient correlation is obtained from the perturbation pressure closure. This novel pressure closure is implemented in an extended EDMF scheme and is shown to successfully simulate a rising bubble as well as shallow and deep convection in a single column model.

Plain Language Summary

Global climate models rely on subgrid-scale (SGS) parameterizations to represent heat and moisture transport by unresolved turbulent and convective motions. In this and two companion papers, the extended eddy-diffusivity mass-flux (EDMF) scheme is developed as a single unified scheme that represents all SGS turbulent and convective processes. This paper focuses on the closure for the perturbation pressure that ensures the non-divergence of the mass flux. An analytical formulation for the pressure closure is derived by considering the dynamics of a buoyant bubble. The closure differs from commonly used formulations in two respects. First, it introduces an additional momentum advection damping term that contributes a momentum source at the bubble bottom and cloud base. Second, it improves the drag term and enables the EDMF scheme to correctly reproduce the diurnal cycle of deep convection. Comparison with large-eddy simulations of moist convection and rising bubbles demonstrates the adequacy of the closure.

1 Introduction

Turbulent and convective motions play essential roles in the transport of energy and moisture in the climate system. Due to computational constraints, climate models use resolutions that are too coarse to resolve these motions and rely heavily on various parameterizations to represent their subgrid-scale (SGS) contribution to the resolved flow. Such parameterizations are one of the primary sources of model uncertainty in long-term climate projections (Bony & Dufresne, 2005; Bony et al., 2015; Brient & Schneider, 2016; Caldwell et al., 2018; Ceppi et al., 2017; Murphy et al., 2004; Teixeira et al., 2011; Webb et al., 2013). Since advances in computational resources will not suffice to fully resolve turbulent and convective motions in the foreseeable future (Schneider et al., 2017), continuous efforts to reduce the biases and uncertainties from SGS parameterizations in climate models are required.

Conventionally, SGS processes such as boundary layer turbulence, shallow convection, and deep convection have been represented by separate parameterization schemes. This leads to a discontinuous representation of processes that lie on a physical continuum. It also results in a proliferation of correlated parameters (e.g., separate entrainment rates for shallow and deep convection), which complicates the calibration of climate models. Considerable efforts have been made to develop a unified parameteriza-

tion that synthesizes the SGS turbulence and convection processes into one single scheme, without artificial switches between different regimes (Lappen & Randall, 2001a, 2001c, 2001b; Larson & Golaz, 2005; Golaz et al., 2002b, 2002a; Soares et al., 2004; Siebesma et al., 2007; Park, 2014a, 2014b; Tan et al., 2018; Thuburn et al., 2018, 2019; Weller & McIntyre, 2019; Cohen et al., 2020; Lopez-Gomez et al., 2020). A challenge in the development of such a unified scheme is closing the representation of various physical processes that emerge in the development of the scheme. In the case of mass-flux parameterizations, one of the key terms requiring closure is the perturbation pressure gradient, which is the focus of this work.

Perturbation pressure, defined as the departure of pressure from a reference profile in hydrostatic balance with a reference density, plays an important role in the development of convective systems (Holton, 1973; Schumann & Moeng, 1991; Jeevanjee & Romps, 2015, 2016; Morrison, 2016b; Peters, 2016). It is an essential source/sink term for vertical momentum (Holton, 1973) and contributes to the redistribution of turbulence kinetic energy (TKE) (Heinze et al., 2015). It is typically diagnosed from a 3D Poisson equation in large-eddy simulations (LES). Its closure remains challenging for parameterization schemes (Holland & Rasmusson, 1973; Morrison, 2016b; Peters, 2016; Tarshish et al., 2018).

Theoretical studies (e.g., Holton (1973); Lappen and Randall (2006); Morrison (2016b, 2016a); Leger et al. (2019)) explicitly solve for the perturbation pressure from a set of differential equations considering both horizontal and vertical motions; they have demonstrated success in idealized simulations. Most parameterization schemes, however, do not explicitly solve for the pressure gradient term from differential equations. Instead, the perturbation pressure gradient is formulated semi-empirically as a combination of various physical processes: a virtual mass effect that effectively reduces buoyancy, a momentum sink proportional to entrainment, and a drag term inversely proportional to the horizontal scale of the updraft (Simpson & Wiggert, 1969; Siebesma et al., 2007; de Roode et al., 2012; Tan et al., 2018; Han & Bretherton, 2019; Suselj et al., 2019).

The formulation of de Roode et al. (2012) represents a pure sink for the vertical momentum of convective systems. However, in an LES study, Jeevanjee and Romps (2015) decomposed the perturbation pressure into a buoyancy perturbation pressure and a dynamic perturbation pressure. They showed that the dynamic pressure is a significant momentum source at low levels of convective systems. Peters (2016) observed a similar positive momentum forcing from the dynamic perturbation pressure in a deep convective system. While the pressure gradient structure can become more complex when the updraft consists of multiple distinct thermals (Moser & Lasher-Trapp, 2017; Morrison et al., 2020), these observed results are in contradiction to the typical pressure closures that serve merely as momentum sinks. In this paper, we demonstrate that a vertical momentum source owing to the perturbation pressure gradient is important for capturing the dynamics of an idealized rising dry bubble.

We derive a novel closure for the perturbation pressure in the extended eddy-diffusivity mass-flux (EDMF) framework (Tan et al., 2018; Cohen et al., 2020). The closure explicitly recognizes the roles of the perturbation pressure as a vertical momentum source and sink and in TKE redistribution. The extended EDMF framework and its entrainment and detrainment closures are presented in Cohen et al. (2020), and the eddy diffusivity and mixing length closures are discussed in Lopez-Gomez et al. (2020). Together with the perturbation pressure closure, these closures make the extended EDMF a unified framework that successfully simulates a wide range of turbulent and convective regimes, from stable boundary layers to deep convection, without altering any of the equation components or parameter values. Moreover, we show here that the extended EDMF scheme is also able to simulate individual convective 2D bubbles, albeit with changes in parameters and some additions to the formulation of the entrainment and detrainment closures.

116 The need for these changes is discussed in the context of the general difference between
 117 convective updrafts and convective bubbles.

118 Section 2 lays out the analytical derivation for the perturbation pressure in a 2D
 119 thermal bubble, with the 3D axisymmetric counterpart given in Appendix B. Section
 120 3 briefly reviews the extended EDMF framework and implements the perturbation pres-
 121 sure closure in it. Section 4 describes the setups of a dry bubble experiment and moist
 122 convective test cases in LES and a single column model (SCM). Simulation results are
 123 shown in Section 5, their implications and limitations are discussed in Section 6. Finally,
 124 Section 7 summarizes the conclusions.

125 2 Vertical Perturbation Pressure Gradient

126 In order to decouple the derivation of the perturbation pressure structure from den-
 127 sity changes, we use the Boussinesq approximation. (Caveats to this approach are dis-
 128 cussed in Section 2.1.) The momentum equation in the Boussinesq approximation is writ-
 129 ten as

$$\frac{\partial \mathbf{v}}{\partial t} + \mathbf{v} \cdot \nabla \mathbf{v} = b \hat{\mathbf{k}} - \nabla \left(\frac{p^\dagger}{\rho_h} \right) + S_{\mathbf{v}}, \quad (1)$$

where t is time, $\mathbf{v} = (u, v, w)$ is the 3D velocity vector, $\hat{\mathbf{k}}$ is the vertical unit vector, ρ_h
 is a constant reference density, and $S_{\mathbf{v}}$ represents 3D momentum sources other than buoy-
 ancy and the pressure gradient force. The buoyancy is defined as

$$b = -g \frac{\rho - \rho_h}{\rho_h},$$

where g is the gravitational acceleration. The perturbation pressure is defined as

$$p^\dagger = p - p_h,$$

130 where $p_h(z)$ is the reference pressure profile in hydrostatic balance with the reference den-
 131 sity ρ_h , i.e., $\hat{\mathbf{k}} \cdot \nabla p_h = -\rho_h g$. Note that ρ_h is a constant reference density, while p_h is
 132 height dependent.

133 2.1 Pressure Poisson Equation

The Boussinesq approximation implies that the velocity \mathbf{v} is nondivergent. There-
 fore, taking the divergence of the momentum equation (1) and ignoring the source term
 $S_{\mathbf{v}}$ leads to a Poisson equation for the perturbation pressure

$$\nabla^2 \left(\frac{p^\dagger}{\rho_h} \right) = \frac{\partial b}{\partial z} - \nabla \cdot (\mathbf{v} \cdot \nabla \mathbf{v}). \quad (2)$$

To simplify notation, we define a pressure potential as

$$P = \frac{p}{\rho_h}. \quad (3)$$

134 In the remainder of this paper, we use the pressure potential P , which we generally re-
 135 fer to as “pressure” as it plays a similar role in the vertical momentum equation. We de-
 136 rive a closure for the gradient of the perturbation pressure potential, ∇P^\dagger , with the dag-
 137 ger again denoting perturbations relative to the reference pressure potential.

It is common to decompose the perturbation pressure into the buoyancy pertur-
 bation pressure (P_b) and the dynamic perturbation pressure (P_d) (i.e., $P^\dagger = P_b + P_d$),

associated with the two terms on the right-hand side of (2),

$$\nabla^2 P_b = \frac{\partial b}{\partial z}, \quad (4a)$$

$$\nabla^2 P_d = - \left[\left(\frac{\partial u}{\partial x} \right)^2 + \left(\frac{\partial v}{\partial y} \right)^2 + \left(\frac{\partial w}{\partial z} \right)^2 \right] - 2 \left[\frac{\partial u}{\partial y} \frac{\partial v}{\partial x} + \frac{\partial v}{\partial z} \frac{\partial w}{\partial y} + \frac{\partial w}{\partial x} \frac{\partial u}{\partial z} \right]. \quad (4b)$$

In the derivations that follow, we consider for simplicity a 2D Cartesian geometry. An analogous derivation for an axisymmetric thermal bubble in cylindrical coordinates is given in Appendix B. In the 2D geometry, with $\mathbf{v} = (u, w)$ and $\nabla_{x,z}^2 = \partial^2/\partial x^2 + \partial^2/\partial z^2$, the Poisson equations (4), after using the continuity equation, become

$$\nabla_{x,z}^2 P_b = \frac{\partial b}{\partial z}, \quad (5a)$$

$$\nabla_{x,z}^2 P_d = -2 \left[\left(\frac{\partial w}{\partial z} \right)^2 + \frac{\partial u}{\partial z} \frac{\partial w}{\partial x} \right]. \quad (5b)$$

138 Considerable efforts have been made to understand the buoyancy perturbation pres-
 139 sure and its impact on the effective buoyancy (Jeevanjee & Romps, 2015; Peters, 2016;
 140 Tarshish et al., 2018). For example, Tarshish et al. (2018) draw analogies between the
 141 effective buoyancy and buoyancy perturbation pressure of the fluid and the magnetic charge
 142 and potential in magnetostatics. They obtain an analytical solution for the buoyancy
 143 perturbation pressure from a homogeneous thermal with added randomness. However,
 144 they do not account for the dynamic perturbation pressure induced by the velocity field.

145 Here we solve the pressure Poisson equation accounting for both the buoyancy and
 146 the dynamic perturbation pressure. We consider a thermal bubble and make a single-
 147 normal mode assumption. Although the single-normal mode assumption is made for sim-
 148 plicity, it has proven to be successful in simulating convective systems. For example, Holton
 149 (1973) adopted a single-normal mode for the horizontal direction when solving for the
 150 perturbation pressure from a diagnostic Poisson equation. Morrison (2016b) derived a
 151 single-normal mode solution for the buoyancy perturbation pressure, making the assump-
 152 tion that the dynamic perturbation pressure is negligible when determining the verti-
 153 cal velocity within an updraft. They also derived a general solution for perturbation pres-
 154 sure from the steady-state momentum and mass continuity equations in presence of a
 155 lower boundary. The derivation in Morrison (2016b) shows a dependency of the pres-
 156 sure forcing term on the dimensionality of the convection: the pressure forcing is stronger
 157 in a 2D Cartesian setup than that in the 3D axisymmetric setup. Here we use the single-
 158 normal mode solution within an ensemble of multiple thermals.

159 The Boussinesq approximation is a limitation to study deep convection. Morrison
 160 (2016a) showed that although the net perturbation pressure between the cloud top and
 161 bottom differs in the Boussinesq and anelastic approximations, the vertical acceleration
 162 is much less sensitive to the approximations. This is due to compensation from the dif-
 163 ferent density profiles used in the two approximations. This provides one justification
 164 for our use of the simplifying Boussinesq approximation.

165 2.2 Single-Normal Mode Solution

In this subsection, we derive a single-normal mode solution for the perturbation pressure for a 2D thermal in Cartesian coordinates. We assume the 2D thermal is positively buoyant and has horizontal extent $2R$ and vertical extent H . That is, its horizontal and vertical wavenumbers are $k_b = \pi/(2R)$ and $m = \pi/H$, respectively. The single-normal mode structure for buoyancy is

$$b = b_A \sin(mz) \cos(k_b x), \quad x \in [-R, R], \quad z \in [0, H], \quad (6)$$

166 where b_A is the normal mode amplitude for buoyancy.

We make a similar single-normal mode ansatz for the flow inside the thermal, assuming free-slip boundary conditions, that is, the vertical velocity w vanishes at the top and bottom of the thermal and the horizontal velocity u vanishes at its lateral boundaries. This configuration defines a closed circulation with an upward branch at the center of the thermal and two outlying descending branches. The velocity field has the same vertical wavenumber as the buoyancy, while its horizontal wavenumber k_w is different from k_b . The single-normal mode structure for vertical velocity is

$$w = w_A \sin(mz) \cos(k_w x), \quad (7)$$

where w_A is the normal mode amplitude for w . From the continuity equation, $\partial_x u + \partial_z w = 0$, we have

$$\frac{\partial u}{\partial x} = -\frac{\partial w}{\partial z} = -mw_A \cos(mz) \cos(k_w x), \quad (8)$$

and we set

$$u = u_A \cos(mz) \sin(k_w x), \quad (9)$$

where u_A is the normal mode amplitude for u . The free-slip boundary condition requires $k_w = 2k_b = \pi/R$; Eqs. (8) and (9) then imply

$$k_w u_A = -mw_A. \quad (10)$$

167 Equations (6), (7), and (9) together describe the single-normal mode structure of
 168 the buoyancy and velocity fields for the 2D thermal in Cartesian coordinates. The flow
 169 pattern that arises is shown in Figure 1. The buoyancy structure and flow fields for a
 170 3D axisymmetric thermal in cylindrical coordinates using the Fourier-Bessel decompo-
 171 sition (Holton, 1973) are described in Appendix B.

172 **2.2.1 Buoyancy Perturbation Pressure**

With the normal-mode ansatz (6), the P_b Poisson equation (5a) reduces to

$$\nabla_{x,z}^2 P_b = \frac{\partial b}{\partial z} = mb_A \cos(mz) \cos(k_b x). \quad (11)$$

The buoyancy perturbation pressure P_b then needs to have the same trigonometric structure as the right-hand side of (11), i.e.,

$$P_b = P_0 \cos(mz) \cos(k_b x). \quad (12)$$

The coefficient P_0 is obtained by substituting this form for P_b into (11), leading to

$$\nabla_{x,z}^2 P_b = -P_0 (m^2 + k_b^2) \cos(mz) \cos(k_b x) = mb_A \cos(mz) \cos(k_b x).$$

This gives

$$P_0 = -\frac{m}{m^2 + k_b^2} b_A.$$

Therefore, the single-normal mode solution for the buoyancy perturbation pressure is

$$P_b = -\frac{m}{m^2 + k_b^2} b_A \cos(mz) \cos(k_b x), \quad (13)$$

and the buoyancy perturbation pressure gradient needed in the vertical momentum equation is

$$-\frac{\partial P_b}{\partial z} = -\frac{m^2}{m^2 + k_b^2} b_A \sin(mz) \cos(k_b x) = -\frac{b}{[1 + (H/2R)^2]}. \quad (14)$$

173 As the bubble gets wider and shallower, a stronger virtual mass effect leads to a
 174 weaker effective buoyancy, consistent with the solution for an idealized spherical bub-
 175 ble with homogeneous buoyancy distribution (Tarshish et al., 2018).

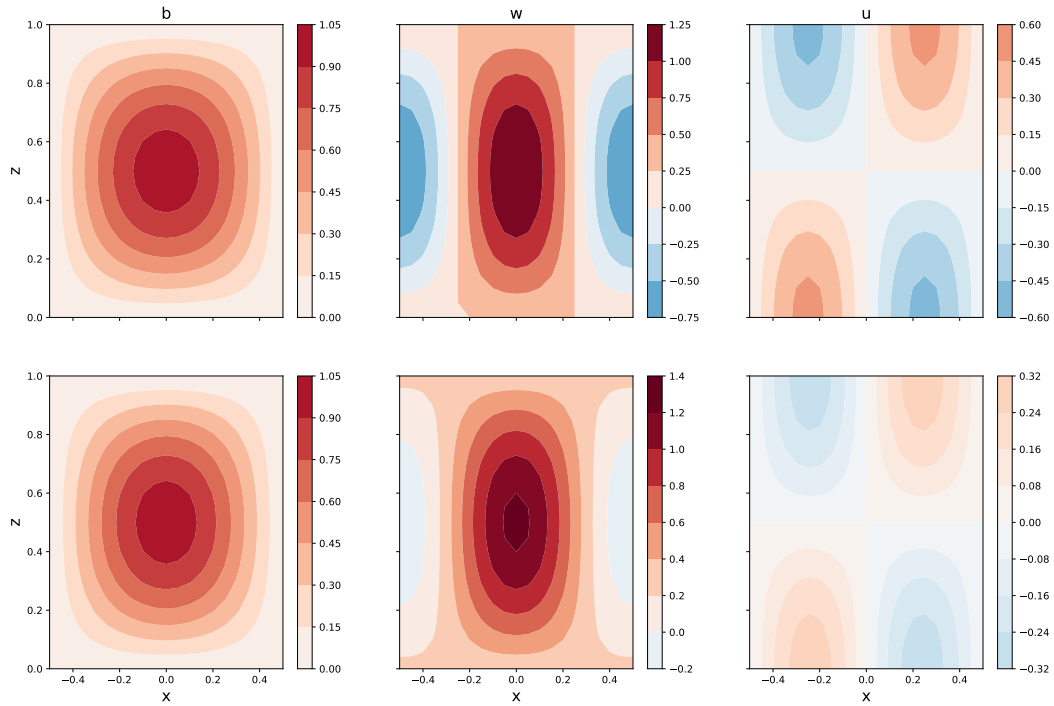


Figure 1. Buoyancy and velocity patterns for the single-normal mode ansatz for the 2D (top) and 3D (bottom) thermals. The thermal is created by specifying dimensionless parameters $2R = H = 1$ and $b_A = w_A = 1$. The velocity amplitude u_A is computed from the non-divergence criterion $k_w u_A + m w_A = 0$. The vertical velocities w in the middle column is shown the velocity from the single-normal model ansatz plus the velocity of the thermal, which is taken as 25% of the peak w at the thermal center.

2.2.2 Dynamic Perturbation Pressure

Similarly, using the ansatz (7) and (9), the Poisson equation for the dynamical pressure becomes

$$\nabla_{x,z}^2 P_d = -2 \left[\left(\frac{\partial w}{\partial z} \right)^2 + \frac{\partial u}{\partial z} \frac{\partial w}{\partial x} \right] = -m^2 w_A^2 \cos(2mz) - m^2 w_A^2 \cos(2k_w x). \quad (15)$$

We assume the dynamic perturbation pressure has the form

$$P_d = P_1 \cos(2mz) + P_2 \cos(2k_w x) + Fz + G(x, xz), \quad (16)$$

which satisfies (15). The function $G(x, xz)$ can be written in the general form $G_1 x + G_2 xz + G_3$. Since the flow is symmetric with respect to $x = 0$, the dynamic perturbation pressure induced by the flow should also be symmetric, i.e., $P_d(x) = P_d(-x)$. As a result, $G_1 = G_2 = 0$, and $G(x, xz) = G_3$ is a constant. Then the Laplacian of P_d is

$$\nabla_{x,z}^2 P_d = -4m^2 P_1 \cos(2mz) - 4k_w^2 P_2 \cos(2k_w x),$$

which gives $P_1 = w_A^2/4$ and $P_2 = m^2 w_A^2/(4k_w^2)$. Therefore, the dynamic perturbation pressure is

$$P_d = \underbrace{\frac{w_A^2}{4} \cos(2mz)}_A + \underbrace{\frac{m^2 w_A^2}{4k_w^2} \cos(2k_w x)}_B + \underbrace{Fz}_C + \underbrace{G_3}_D. \quad (17)$$

The ultimate goal is to parameterize the pressure gradient force $-\partial_z P_d$, in which the z -independent terms, B and D , do not participate. Term C in (17) may be used to describe the aerodynamic drag, alleviating the shortcomings of our simplified inviscid approximation. The form drag experienced by the thermal equals the total pressure (air pressure plus $0.5\rho|w|^2$) loss of the surrounding flow across the thermal (Liu et al., 2015), that is,

$$\int_{-R}^R \rho \left[P_d + \frac{w^2}{2} \right]_{z=0}^{z=H} dx = \frac{1}{2} \rho A c_d w_r^2, \quad (18)$$

where c_d is the drag coefficient, A is the cross-sectional area perpendicular to w_r (i.e., $A = 2R$ in the 2D setup), and w_r is the velocity of the thermal relative to the environment. Using P_d from (17) in (18), we obtain

$$F = \frac{1}{2} c_d \frac{w_r^2}{H}, \quad (19)$$

describing the pressure drag the thermal experiences in the fluid. This drag, derived by integrating the total pressure along the boundaries of the thermal, is a result of the particular assumptions we made for the flow pattern and boundary conditions. Finally, the vertical pressure gradient force is given by

$$\begin{aligned} -\frac{\partial P_d}{\partial z} &= \frac{m}{2} w_A^2 \sin(2mz) - \frac{1}{2} c_d \frac{w_r^2}{H} \\ &= m w_A^2 \sin(mz) \cos(mz) - \frac{1}{2} c_d \frac{w_r^2}{H} \\ &= w_A \sin(mz) \frac{d}{dz} [w_A \sin(mz)] - \frac{1}{2} c_d \frac{w_r^2}{H} \\ &= w_c \frac{dw_c}{dz} - \frac{1}{2} c_d \frac{w_r^2}{H}, \end{aligned} \quad (20)$$

where $w_c = w_A \sin(mz)$ represents the velocity at the thermal axis.

The single-normal mode assumption is a major simplification for the thermal structure and has some limitations. It approximates the thermal as a flow perturbation with

180 positive buoyancy and trigonometric structure in both horizontal and vertical directions.
 181 Its implied internal flow has two symmetric circulation lobes, with ascending branch in
 182 the center and descending branches on the sides. This flow pattern resembles the inter-
 183 nal flow within Hill’s vortex (e.g., Levine (1959)), except that it is defined over a rect-
 184 angle instead of a circle.

185 Figure 1 sketches out the buoyancy and velocity fields under this ansatz. Note that
 186 convection consists of a large ensemble of thermals (e.g., Sherwood et al. (2013), Romps
 187 and Charn (2015), Morrison et al. (2020)), and parameterization schemes aim at rep-
 188 resenting the statistical behavior of the ensemble. In Appendix C, we lay out a deriva-
 189 tion for the ensemble composite of multiple thermals centered at their centroids. The
 190 analytical structure for the multi-thermal ensembles, shown in Figure C1, is consistent
 191 with the idealized simulation results in Morrison (2016b) and resembles the composite
 192 results of bubbles identified in the convective test cases (Figure 5).

193 Asymmetries arising from the lower boundaries and from the environment wind shear
 194 can be important in the development and maintenance of convective systems (Jeevanjee
 195 & Romps, 2016; Morrison, 2016b); they are neglected in this idealized symmetric ther-
 196 mal setup.

197 Despite these simplifications, the solutions for the buoyancy perturbation pressure
 198 P_b in (13) and the dynamic perturbation pressure P_d in (17) are consistent with ideal-
 199 ized numerical simulations (Morrison, 2016b; Morrison & Peters, 2018).

200 3 Perturbation Pressure Gradient in the Extended EDMF Scheme

In the EDMF framework, a GCM grid box is divided into subdomains that consist of coherent updrafts/downdrafts and an isotropic environment. Following Cohen et al. (2020), the conditional average of a property ϕ in the i -th subdomain is denoted by $\bar{\phi}_i$, with a_i as the area fraction occupied by the subdomain. The fluctuation around the subdomain average is denoted by $\phi'_i = \phi - \bar{\phi}_i$. We use $i = 0$ for the turbulent isotropic environment and $i \geq 1$ for coherent updrafts and downdrafts. Angle brackets $\langle \phi \rangle$ denote the grid-mean average of ϕ , and $\phi^* = \phi - \langle \phi \rangle$ denotes the fluctuation around the grid mean. It is also convenient to define the difference between the subdomain average and the grid box average as $\bar{\phi}_i^* = \bar{\phi}_i - \langle \phi \rangle$. Finally, the grid box average is related to the subdomain average by the area-weighted average over all subdomains:

$$\langle \phi \rangle = \sum_i a_i \bar{\phi}_i. \tag{21}$$

Using Reynolds averaging rules and this subdomain decomposition, SGS vertical fluxes are decomposed into the sum of subdomain-average components and components owing to fluctuations within the subdomains:

$$\langle w^* \phi^* \rangle = \sum_i a_i (\bar{w}_i^* \bar{\phi}_i^* + \overline{w'_i \phi'_i}). \tag{22}$$

201 The first term is represented by mass flux closures while the second term is taken to be
 202 nonzero only for the turbulent environment ($i = 0$); it is modeled as downgradient eddy
 203 diffusion, hence name of the eddy-diffusivity mass-flux (EDMF) scheme. Accurate pa-
 204 rameterization of this SGS vertical flux is the key goal of the EDMF scheme.

205 The full set of equations solved by the extended EDMF scheme is discussed in Cohen
 206 et al. (2020). For the purpose of understanding the role of perturbation pressure, here
 207 we briefly lay out the vertical momentum equation for updrafts/downdrafts, and the TKE
 208 equation for the environment, in which the perturbation pressure arises.

209
 210

3.1 Updraft Vertical Velocity and Environmental TKE in the Extended EDMF Scheme

The vertical momentum equation for the i -th subdomain is

$$\begin{aligned}
 \frac{\partial(\rho a_i \bar{w}_i)}{\partial t} + \nabla_h \cdot (\rho a_i \langle \mathbf{u}_h \rangle \bar{w}_i) + \frac{\partial(\rho a_i \bar{w}_i \bar{w}_i)}{\partial z} &= \underbrace{\frac{\partial}{\partial z} \left(\rho a_i K_{w,i} \frac{\partial \bar{w}_i}{\partial z} \right)}_{\text{turbulent flux}} \\
 + \underbrace{\sum_{j \neq i} \left[(E_{ij} + \hat{E}_{ij}) \bar{w}_j - (\Delta_{ij} + \hat{\Delta}_{ij}) \bar{w}_i \right]}_{\text{entrainment/detrainment}} &+ \underbrace{\rho a_i \bar{b}_i^* + \rho a_i \langle b \rangle}_{\text{buoyancy}} \\
 - \underbrace{\rho a_i \left(\frac{\partial P^\dagger}{\partial z} \right)_i^* - \rho a_i \frac{\partial \langle P^\dagger \rangle}{\partial z}}_{\text{perturbation pressure}}, & \tag{23}
 \end{aligned}$$

 211
 212
 213
 214
 215
 216

where \mathbf{u}_h is the horizontal component of the velocity vector, whose subdomain value is taken to be equal to its grid-mean value. Following Cohen et al. (2020), $\rho = \langle \rho \rangle$ is the grid-mean density. The exchange of mass is represented by dynamical entrainment, E_{ij} , dynamical detrainment, Δ_{ij} , and turbulent entrainment, \hat{E}_{ij} ; see Cohen et al. (2020) for details. Vertical turbulent fluxes are represented by the eddy diffusivity $K_{w,i}$ (Lopez-Gomez et al., 2020).

The subdomain buoyancy is defined as

$$\bar{b}_i = -g \frac{\bar{\rho}_i - \rho_h}{\rho}.$$

It is decomposed into a contribution from the grid-mean buoyancy

$$\langle b \rangle = -g \frac{\rho - \rho_h}{\rho},$$

and a departure from the grid mean

$$\bar{b}_i^* = -g \frac{\bar{\rho}_i^* - \rho_h}{\rho}.$$

Similarly, the perturbation pressure gradient is decomposed into a grid-mean component and a departure from the grid mean, i.e.,

$$-\left(\frac{\partial P^\dagger}{\partial z} \right)_i = -\frac{\partial \langle P^\dagger \rangle}{\partial z} - \left(\frac{\partial P^\dagger}{\partial z} \right)_i^*. \tag{24}$$

 217
 218
 219
 220
 221
 222

In the GCM setting, the grid-mean buoyancy $\langle b \rangle$ and perturbation pressure gradient $-\partial \langle P^\dagger \rangle / \partial z$ are provided by the dynamical core; in the SCM setting, they are balanced as in Eq. (47) in Cohen et al. (2020). The subdomain buoyancy relative to the grid mean, \bar{b}_i^* , is computed from the density using a nonlinear saturation adjustment; see the appendix in Pressel et al. (2015). Here we develop a closure scheme for the subdomain perturbation pressure, $-\left(\partial P^\dagger / \partial z \right)_i^*$.

The subdomain TKE is defined as $\bar{e}_i = 0.5(\overline{u_i'^2} + \overline{v_i'^2} + \overline{w_i'^2})$, and the environmental ($i = 0$) TKE equation is

$$\begin{aligned}
 & \frac{\partial(\rho a_0 \bar{e}_0)}{\partial t} + \nabla_h \cdot (\rho a_0 \langle \mathbf{u}_h \rangle \bar{e}_0) + \frac{\partial(\rho a_0 \bar{w}_0 \bar{e}_0)}{\partial z} = \\
 & \underbrace{\frac{\partial}{\partial z} \left(\rho a_0 K_{m,0} \frac{\partial \bar{e}_0}{\partial z} \right)}_{\text{turbulent transport}} + \underbrace{\rho a_0 K_{m,0} \left[\left(\frac{\partial \langle u \rangle}{\partial z} \right)^2 + \left(\frac{\partial \langle v \rangle}{\partial z} \right)^2 + \left(\frac{\partial \bar{w}_0}{\partial z} \right)^2 \right]}_{\text{shear production}} \\
 & + \sum_{i>0} \left(\underbrace{-\hat{E}_{0i} \bar{e}_0}_{\text{turb. entrainment}} + \underbrace{\bar{w}_0^* \hat{E}_{0i} (\bar{w}_0 - \bar{w}_i)}_{\text{turb. entrainment production}} \right) \\
 & + \sum_{i>0} \left(\underbrace{-\Delta_{0i} \bar{e}_0}_{\text{dyn. detrainment}} + \underbrace{\frac{1}{2} E_{0i} (\bar{w}_0 - \bar{w}_i) (\bar{w}_0 - \bar{w}_i)}_{\text{dyn. entrainment production}} \right) \\
 & + \underbrace{\rho a_0 \overline{w_0' b_0'}}_{\text{buoyancy production}} - \underbrace{\rho a_0 \left[u_0' \left(\frac{\partial P^\dagger}{\partial x} \right)'_0 + v_0' \left(\frac{\partial P^\dagger}{\partial y} \right)'_0 + w_0' \left(\frac{\partial P^\dagger}{\partial z} \right)'_0 \right]}_{\text{pressure work}} - \underbrace{\rho a_0 \bar{D}_{e,0}}_{\text{dissipation}}, \quad (25)
 \end{aligned}$$

223 with TKE dissipation denoted by $\bar{D}_{e,0}$. Closure schemes for the shear production, en-
 224 trainment and detrainment, turbulent transport, buoyancy production, and dissipation
 225 are discussed in Cohen et al. (2020) and Lopez-Gomez et al. (2020).

The pressure work in the environment can be computed using

$$-\rho a_0 \left[w_0' \left(\frac{\partial P^\dagger}{\partial z} \right)'_0 + u_0' \left(\frac{\partial P^\dagger}{\partial x} \right)'_0 + v_0' \left(\frac{\partial P^\dagger}{\partial y} \right)'_0 \right] = \sum_{i \geq 1} \rho a_i (\bar{w}_i^* - \bar{w}_0^*) \overline{\left(\frac{\partial P^\dagger}{\partial z} \right)'_i}, \quad (26)$$

226 once the perturbation pressure gradient is closed for the momentum equations in the up-
 227 drafts and downdrafts. This equation assumes that subdomain covariances within up-
 228 drafts and downdrafts are negligible, a general assumption in EDMF schemes. A deriva-
 229 tion of this relation is provided in Appendix A, given the assumption that pressure per-
 230 turbations only redistribute TKE between subdomains and do no work on the grid mean
 231 (Tan et al., 2018). It is noteworthy that (26) is different from how the pressure work term
 232 is closed in many higher-order turbulence schemes (e.g., Bretherton and Park (2009)),
 233 which usually combine the pressure work with the turbulent TKE transport and param-
 234 eterize the resulting combined term diffusively.

235 3.2 Implementation of Perturbation Pressure Closure in the Extended 236 EDMF Scheme

Equations (14) and (20) provide the buoyancy and dynamic perturbation pressure forcing in the 2D single-normal mode flow. They apply to the pointwise vertical momentum equation within a thermal. To derive expressions similar to (14) and (20) that are suitable for implementation in the EDMF scheme, we take updrafts in the EDMF scheme to be ensembles of thermals as discussed in Appendix C, and we conditionally average over the thermals, obtaining for scalar fluxes

$$\bar{w}_i \bar{\phi}_i = \left(\frac{1}{\sum_{j=1}^N 2R_j} \right) \sum_{j=1}^N \int_{-R_j}^{R_j} w \phi d\tilde{x} = \sum_{j=1}^N \frac{a_j^T}{a_i} \{w\phi\}_j. \quad (27)$$

Here, i represents the i -th subdomain in the EDMF scheme, j represents the j -th thermal in the i -th subdomain, \tilde{x} is a local coordinate centered on each thermal axis, R_j is the horizontal radius of the j -th thermal, a_j^T is the area fraction of the j -th thermal, and the $\{\cdot\}_j$ operator represents the average over the j -th thermal. In the EDMF framework, it is assumed that variance within updrafts is negligible, and the vertical transport of

heat $(\overline{w_i b_i})$, or of any other tracer, is achieved through the updraft mean properties $(\overline{w_i}$ and $\overline{b_i})$, that is,

$$\frac{1}{V} \int_{\Omega_i} w b dV = \overline{w_i} \overline{b_i}. \quad (28)$$

237 Here, Ω_i represents the i -th subdomain within a grid box. To apply this to the thermal
 238 ensemble, the thermal-mean buoyancy (and other scalars except w) is taken as the av-
 239 erage over the thermal, while the effective $\overline{w_i}$ is obtained from expression (28).

Applying the conditional average to the buoyancy perturbation pressure gradient as in (15), the buoyancy perturbation pressure gradient force for the i -th updraft, consisting of N thermals, is

$$-\left(\frac{\partial P_b}{\partial z}\right)_i = -\sum_{j=1}^N \frac{a_j^T}{a_i} \frac{1}{1 + \left(\frac{H_j}{2R_j}\right)^2} \{b\}_j, \quad (29)$$

240 This virtual mass effect reduces the effective buoyancy of the thermal with respect to
 241 the buoyancy computed from density fluctuations (Davies-Jones, 2003; Jeevanjee & Romps,
 242 2015). Consistent with LES simulations (Romps & Charn, 2015; Tarshish et al., 2018),
 243 the virtual mass contribution depends on the aspect ratio, $2R/H$, of the convective sys-
 244 tem.

Assuming each thermal contributes almost equally to the updraft buoyancy (i.e., $a_j^T \{b\}_j / a_i = \eta \overline{b_i}$) and that the inverse aspect ratio $\hat{\alpha} = H/2R$ of thermals ranges uniformly from 0 to a certain value $\hat{\alpha}_m$, equation (29) can be approximated as

$$-\left(\frac{\partial P_b}{\partial z}\right)_i = -\sum_{j=1}^N \frac{\eta \overline{b_i}}{1 + \left(\frac{H_j}{2R_j}\right)^2} \approx -\frac{N}{\hat{\alpha}_m} \int_0^{\hat{\alpha}_m} \frac{1}{1 + \hat{\alpha}^2} \eta \overline{b_i} d\hat{\alpha} = -\frac{N\eta}{\hat{\alpha}_m} \arctan(\hat{\alpha}_m) \overline{b_i}. \quad (30)$$

245 The $\arctan(\hat{\alpha}_m)$ function behaves as an activation function in terms of the maximum
 246 inverse aspect ratio $\hat{\alpha}_m$ of the thermals sustaining convection. It easily saturates (i.e.,
 247 is constantly activated) for reasonable convective aspect ratios. Considering the steeper
 248 part of the $\arctan(\hat{\alpha}_m)$ function might be important for high spatial resolutions, where
 249 there are fewer thermals within a grid box. In the EDMF implementation, we use ex-
 250 pression (30) to diagnose the departure from the grid mean following (24).

251 The implementation of the dynamic perturbation pressure gradient in the EDMF
 252 scheme requires an effective vertical velocity $\overline{w_i}$, defined by (28). Consider a simplified
 253 case with a single thermal and let $w_c(z) = w_A \sin(mz)$ and $b_c(z) = b_A \sin(mz)$ rep-
 254 resent the vertical velocity and buoyancy at the thermal axis. Following (28),

$$\overline{w_i} \overline{b_i} = \frac{1}{2R} \int_{-R}^R w_c \cos(2k_b x) b_c \cos(k_b x) dx = \frac{2}{3\pi} w_c b_c, \quad (31)$$

255 and thus the updraft velocity $\overline{w_i}$ is proportional to the vertical velocity at the axis of the
 256 thermal when considering one thermal. Writing $\overline{w_i}^* = \gamma w_{c,j}$, applying the conditional
 257 average on the advection damping term in (20), and diagnosing the pressure drag from
 258 the pressure deficit across the thermal ensemble yields the dynamic perturbation pres-
 259 sure gradient for the updraft

$$-\left(\frac{\partial P_d}{\partial z}\right)_i^* = \frac{1}{\gamma^2} \overline{w_i}^* \frac{d\overline{w_i}^*}{dz} - \frac{1}{2} c_d \frac{w_{r,i}^2}{H_i} = \alpha_a \overline{w_i}^* \frac{d\overline{w_i}^*}{dz} - \frac{1}{2} c_d \frac{w_{r,i}^2}{H_i}. \quad (32)$$

260 The first term on the right-hand side counteracts the advection of vertical momen-
 261 tum in (23). The parameter $\alpha_a = \gamma^{-2}$ is a scaling parameter that describes the advec-
 262 tion damping strength. This term stands out as the only term that can serve as a source

263 of momentum in a buoyant thermal bubble; the resulting acceleration in the lower half
 264 of the bubble is an important term in the vertical momentum budget. It is tightly con-
 265 nected to the vertical structure of P_d , as indicated by the first term on the right-hand
 266 side of (17). The dynamic perturbation pressure attributed to this term has high pres-
 267 sure centered at the top and bottom of the thermal and low pressure centered at the ther-
 268 mal center, consistent with the dynamic pressure structure from numerical simulations
 269 of an idealized thermal bubble (Peters, 2016; Morrison & Peters, 2018) and the multi-
 270 mode ensemble of thermal structures as shown in Figure C1.

271 By contrast, the simplification via the single-normal mode ansatz leads to a ver-
 272 tically symmetric structure with respect to the thermal center (similar to Hill’s vortex),
 273 whereas the numerical simulations in Morrison and Peters (2018) demonstrate some asym-
 274 metry. As discussed in Peters (2016), the high pressure at the top and bottom is related
 275 to the $-(\partial_x u)^2 - (\partial_z w)^2$ term in the Poisson equation (4), and it partially compensates
 276 the divergence of the flow. The low pressure in the center is related to the $-(\partial_z u)\partial_x w$
 277 term in the Poisson equation and comes from the vortex ring-like structure. This high-
 278 low-high vertical pattern leads to an upward pressure gradient force in the lower half of
 279 the thermal and a downward force in the upper half, counteracting the momentum ad-
 280 vection in the \bar{w}_i prognostic equation.

The second term in (32) represents a form drag, a necessary correction to the sim-
 plified configuration given by free-slip boundary conditions between thermals and the
 environment. In the EDMF scheme, a z -dependent relative velocity is computed as $w_{r,i} =$
 $\bar{w}_i - \bar{w}_0$, and thus, the drag term is defined as

$$-\alpha_d \frac{(\bar{w}_i^* - \bar{w}_0^*)|\bar{w}_i^* - \bar{w}_0^*|}{H_i}, \quad (33)$$

281 where the subscript i represents the i -th updraft/downdraft and 0 represents the envi-
 282 ronment. The velocity $\bar{w}_i^* - \bar{w}_0^*$ is the relative velocity between the updraft/downdraft
 283 and the environment (with the grid mean $\langle w \rangle$ removed from both \bar{w}_i and \bar{w}_0). For sim-
 284 plicity, the factor 1/2 in the derivations of the drag is subsumed into the parameter α_d ,
 285 which we later adjust empirically. Note that the squared velocity has been substituted
 286 by a product with its absolute value, consistent with the fact that for a downdraft the
 287 total pressure difference between $z = H$ and $z = 0$ has opposite sign.

288 The drag term (33) is different from commonly adopted drag terms (e.g., Simpson
 289 and Wiggert (1969); de Roode et al. (2012); Tan et al. (2018)) in two respects: First, it
 290 uses the relative velocity between the drafts and the environment instead of the updraft
 291 velocity, which is applicable for large updraft area fractions; second, it uses a $1/H$ scal-
 292 ing instead of the $1/R$ scaling, which we found to be crucial for the diurnal cycle of deep
 293 convection.

As shown in Appendix B, for the axisymmetric thermal, contributions to the per-
 turbation pressure gradient can also be decomposed into virtual mass, advection damp-
 ing, and drag, with the main difference being the scaling parameters that arise. There-
 fore, the pressure gradient force for the i -th EDMF subdomain can be generalized as

$$-\left(\frac{\partial P^\dagger}{\partial z}\right)_i^* = -\alpha_b \bar{b}_i^* + \alpha_a \bar{w}_i^* \frac{\partial \bar{w}_i^*}{\partial z} - \alpha_d \frac{(\bar{w}_i^* - \bar{w}_0^*)|\bar{w}_i^* - \bar{w}_0^*|}{\min(H_i, 500 \text{ m})}, \quad (34)$$

294 where α_b , α_a , and α_d are dimensionless parameters that describe the contributions from
 295 the virtual mass effect, advection damping, and pressure drag. A minimum length scale
 296 of 500 m is used to avoid a vanishing denominator. In the examples we show, we tuned
 297 these parameters manually for the scheme to perform across a spectrum of convective
 298 scenarios. A significant change in the drag formula is that the vertical extent of the con-
 299 vective system rather than the horizontal radius (as in Tan et al. (2018) or Simpson et
 300 al. (1965)) is used as the length scale. It is shown in Section 5 that this is a key mod-

301 ification that allows the EDMF scheme to correctly capture the onset of deep convec-
 302 tion.

303 The pressure formulation (34) has three tunable, non-dimensional parameters: a
 304 virtual mass parameter (α_b), an advectivon damping parameter (α_a), and a drag param-
 305 eter (α_d) (in addition to the cutoff length scale). The virtual mass parameter (α_b) is de-
 306 pendent on the number and aspect ratio of thermals sustaining convection, but Eq. (30)
 307 suggests it assumes an approximately fixed value when the number of thermals is large.
 308 The advection damping parameter (α_a) describes a compensation between perturbation
 309 pressure gradient and the momentum advection so that the flow stays non-divergent. The
 310 drag parameter (α_d) modulates the strength of the drag effect. Romps and Charn (2015)
 311 determined the drag coefficient for a spherical thermal to be 0.6. Tan et al. (2018) took
 312 into account this drag formula and adjusted the coefficient for the spherical thermal to
 313 that of a cylindrical plume. However, the drag effect as in Romps and Charn (2015) did
 314 not separate the buoyancy and dynamic contributions. Their drag term represents the
 315 entire pressure gradient force, which is conceptually different from the drag term we de-
 316 rived in (34).

317 While the three parameters have direct physical interpretations, we take them as
 318 empirical parameters to be learned from data. The parameters ($\alpha_b, \alpha_a, \alpha_d$) are a sub-
 319 set of the EDMF parameters, which we obtained sequentially: We first tuned the mix-
 320 ing length parameters with stable boundary layer simulations (Lopez-Gomez et al., 2020),
 321 followed by the entrainment parameters and (α_b, α_a) parameters relevant to dry convec-
 322 tion (Cohen et al., 2020). Finally, we tuned the moisture-dependent detrainment param-
 323 eters and the drag coefficient α_d to reproduce the cloud layer profiles and the cloud top
 324 height in moist convection.

325 4 Experimental Setups in LES and SCM

326 We implemented the extended EDMF framework in the SCM described in Tan et
 327 al. (2018) and Cohen et al. (2020). It uses the liquid potential temperature (θ_l) as the
 328 prognostic thermodynamic variable for both dry and moist experiments. For dry cases,
 329 $\theta_l = \theta$. We take (34) as the pressure closure for the updraft vertical momentum equa-
 330 tion and (26) as the pressure work for the environmental TKE equation. The performance
 331 of the EDMF scheme in the SCM is compared with LES. The LES are performed with
 332 PyCLES (Pressel et al., 2015), an anelastic atmospheric LES code with entropy and to-
 333 tal water specific humidity as prognostic variables, designed to simulate boundary layer
 334 turbulence and convection. We examine the structure of a dry rising bubble following
 335 the benchmark test in Bryan and Fritsch (2002), and also compare our simplified ther-
 336 mal bubble structure to individually selected thermals in observationally motivated test
 337 cases of moist convection.

338 4.1 2D Dry Rising Bubble

339 4.1.1 LES Setup

The dry rising bubble experiment runs on a 2D domain of 10 km in height and 20 km
 in width. The initial liquid water potential temperature (θ_l) distribution over the do-
 main is

$$\theta_l(x, z) = \begin{cases} 300 \text{ K} + (2 \text{ K}) \cos^2(0.5\pi L(x, z)), & \text{if } L < 1, \\ 300 \text{ K}, & \text{if } L \geq 1, \end{cases} \quad (35)$$

where

$$L = \sqrt{\left(\frac{x - x_c}{x_r}\right)^2 + \left(\frac{z - z_c}{z_r}\right)^2} \quad (36)$$

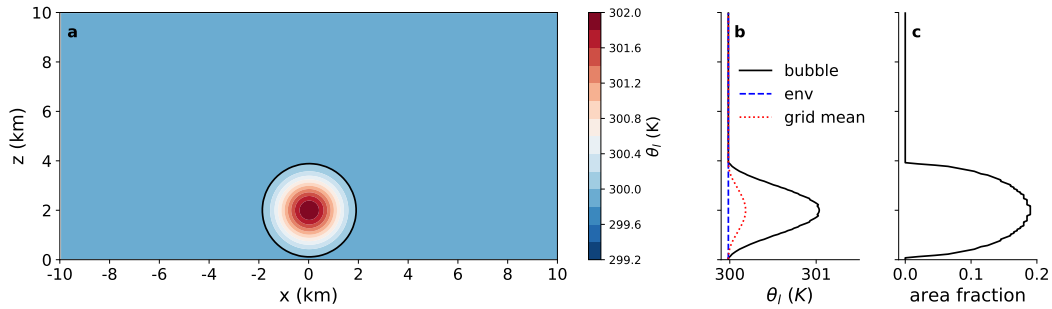


Figure 2. Initial profiles of the rising bubble experiments in LES. (a) Contours of θ_l with intervals of 0.2 K. The black contour is at 300 K and it outlines the edge of the initial bubble that is used for the conditional average computation. (b) Initial vertical profiles of θ_l conditionally averaged over the bubble (black solid line) and the environment (blue dashed line), as well as the grid-mean θ_l (red dotted line). (c) Initial profile of the bubble area fraction.

340 represents the normalized distance from the point (x, z) to the bubble center $x_c = 10$ km
341 and $z_c = 2$ km, and $x_r = z_r = 2$ km represent the initial radius of the bubble. This
342 initial θ_l distribution is unstable near x_c and stable far from it (Figure 2a). The ther-
343 mal bubble contains the strongest warm anomaly in the bubble center, which decays to-
344 ward the edge of the bubble. The liquid water potential temperature θ_l is homogeneous
345 outside the bubble, creating an almost neutral environment. Both the environment and
346 the bubble are initially at rest. The buoyancy force associated with the perturbed θ_l field
347 provides the initial momentum source for the bubble to rise.

348 4.1.2 SCM Setup

349 The SCM simulation is initialized by taking the conditional average over the bubble
350 from the LES initial setup. The buoyant bubble is identified by the 300-K θ_l -contour
351 (black contour in Figure 2a). The initial updraft area fraction is computed as the ratio
352 of the horizontal extent of the bubble over the horizontal LES domain size as shown in
353 Figure 2c. Initial θ_l for the updraft is computed as the conditional average of θ_l within
354 the perturbed area, shown in Figure 2b. Also shown are the grid-mean and environmen-
355 tal profiles of initial θ_l . This initial θ_l profile introduces a positively buoyant bubble into
356 a negatively buoyant environment. The updraft velocity is initialized as zero through-
357 out the column, consistent with the resting initial state in LES. No external forcing is
358 applied along the simulation.

359 As discussed in Cohen et al. (2020), subdomain horizontal velocities are assumed
360 equal to the grid-mean horizontal velocity, and changes in area fraction due to horizon-
361 tal mass exchange are attributed to dynamical entrainment and detrainment. A rising
362 bubble results in a large mass and momentum convergence at the bubble bottom and
363 divergence at the top (Sánchez et al., 1989). This requires an additional divergence term
364 in addition to the dynamical entrainment and detrainment. Therefore, the entrainment
365 and detrainment rates for the bubble test case are modified as

$$E_{ij} = \tilde{E}_{ij} + \rho c_{\text{div}} \max\left(\frac{d(a_i w_i)}{dz}, 0\right), \quad (37)$$

$$\Delta_{ij} = \tilde{\Delta}_{ij} + \rho c_{\text{div}} \max\left(-\frac{d(a_i w_i)}{dz}, 0\right), \quad (38)$$

where $c_{\text{div}} = 0.4$ is a scaling coefficient, and \tilde{E}_{ij} and $\tilde{\Delta}_{ij}$ are the entrainment and detrainment rates proposed by Cohen et al. (2020). The second term is an addition for the bubble test case only; it has been implemented in an EDMF scheme for simulating oceanic convection (Giordani et al., 2020) and a multi-fluid framework for the thermal bubble (Weller et al., 2020). The bubble test case is an initial value problem that is different from the typical boundary value problems for turbulence and convection that a SGS model needs to simulate in a climate model, and hence the introduction of these additional terms, not present in Cohen et al. (2020) and Lopez-Gomez et al. (2020), may be justified. The parameters for the pressure gradient force (34) for the 2D thermal bubble simulation are set to $(\alpha_b, \alpha_a, \alpha_d) = (0.14, 0.4, 0.1)$.

4.2 Moist Convection

Atmospheric convective systems consist of large numbers of thermal bubbles (Moser & Lasher-Trapp, 2017; Hernandez-Deckers & Sherwood, 2016), which can be identified by their dynamical and thermodynamic properties (e.g., Romps and Charn (2015)). Morrison et al. (2020) and Peters et al. (2020) illustrate a more complicated thermal chain structure under certain conditions that links the convective updrafts to starting plumes. A convective parameterization attempts to represent the statistical mean of these bubbles.

We have already shown the EDMF scheme with the proposed pressure closure to be successful in representing various boundary layer regimes, including stratocumulus-topped boundary layers, dry convective boundary layers, and shallow and deep moist convection (Cohen et al., 2020; Lopez-Gomez et al., 2020). Here we present the following two moist convective cases, in which the perturbation pressure gradient is an important forcing term:

- A maritime shallow convection case from the Barbados Oceanographic and Meteorological Experiment (BOMEX, Holland and Rasmusson (1973)). The initial profile and large-scale forcing follow the experiment specifications in Siebesma et al. (2003). We use a $(6.4 \text{ km})^2 \times 3 \text{ km}$ domain with an isotropic resolution of 40 m.
- A continental deep convection case from the Tropical Rainfall Measurement Mission Large-scale Biosphere-Atmosphere experiment (TRMM-LBA, Grabowski et al. (2006)). The initial profile and time-evolving surface fluxes follows the experiment specifications in Grabowski et al. (2006). A warm-rain cutoff scheme is implemented consistently in both LES and SCM. The simulation runs on a $(25.6 \text{ km})^2 \times 22 \text{ km}$ domain with an isotropic resolution of 200 m.

The LES and SCM simulations for BOMEX and TRMM-LBA follow the experimental setups described in Cohen et al. (2020). The pressure closure takes the form (34) with parameters $(\alpha_b, \alpha_a, \alpha_d) = (0.12, 0.1, 10.0)$. (We use different parameters for 2D and 3D cases, as suggested by the derivations in Section 2 and Appendix B.) The closures for entrainment and detrainment are given by Eqs. (31) and (32) in Cohen et al. (2020), that is, without the divergence term as described above for the bubble case. The eddy diffusivity and mixing length in the environment are closed as in Lopez-Gomez et al. (2020). At the same time, the results in these companion papers rely on the pressure closure derived in this work.

Following Couvreux et al. (2010), a passive tracer is added for the LES simulation. A 3D mask that identifies updrafts in moist convection is obtained based on criteria on the vertical velocity, tracer concentration, and liquid water specific humidity as described in Cohen et al. (2020). We compute the bulk properties of convective plumes by taking the conditional average over the updraft mask. Against these bulk properties, we compare the performance of the updraft profiles in the SCM simulations.

414 To investigate the average structure of thermal bubbles in moist convection, we identify
 415 bubbles from the 3D outputs for the last simulation timestep. We search for thermals
 416 as coherent subsets of the updraft structures. To exclude negatively buoyant structures,
 417 which can occur near cloud top in convective overshoots, we remove regions of negative
 418 buoyancy from the tracer-based updraft identification.

419 In BOMEX, thermal bubbles are identified by sweeping over the 3D fields from the
 420 cloud-top level down to cloud-base. For TRMM-LBA, we perform a top-down search for
 421 convective thermals that grow above 3 km. The 3D mask that identifies updrafts in fact
 422 labels isolated clusters that sit at different horizontal and vertical locations of the simulation
 423 domain. At each height level, once a cluster (2D) with at least 3 neighboring grid
 424 cells is located via the updraft identification criteria, this cluster becomes a candidate
 425 to be part of the thermal. Further down in the computational domain, when 2D clusters
 426 identified in a lower level overlap with the clusters identified above, then they are
 427 considered to be part of the same 3D thermal. Once such 3D thermal elements have been
 428 identified, those with horizontal or vertical scales smaller than 5 grid cells are excluded
 429 from the analysis, to avoid randomness from small structures. In the end, we identify
 430 13 convective thermals from BOMEX and 8 from TRMM-LBA for a composite study.
 431 Various more complicated thermal tracking algorithms are available (e.g., (Romps & Charn,
 432 2015; Hernandez-Deckers & Sherwood, 2016; Morrison et al., 2021)). These take into consideration
 433 flow structures and their time evolution and investigate the time-evolving characteristics
 434 of the thermals. This is beyond the scope of this work. Our aim merely is to compare
 435 our solution for the perturbation pressure against thermals in LES snapshots.

436 A composite of the thermal bubbles is created to illustrate their robust structures
 437 in w , buoyancy, P^\dagger and $-\partial_z P^\dagger$. First, for each bubble, the location of the maximum w
 438 is identified as the reference grid point for the composite analysis. Then, an azimuthal
 439 average is computed around the vertical axis that goes through the location of the maximum
 440 w in the bubble. Finally, the composite is created by aligning the 2D azimuthal
 441 averages of each bubble by their locations of maximum w .

442 5 Results

443 5.1 2D Rising Bubble

444 Snapshots of the bubble structure from LES are shown in Figure 3. Similar to Figure
 445 2a, the bubble is outlined by black contours with zero buoyancy. Given this initial
 446 buoyancy distribution, the upward vertical velocity builds up quickly inside the bubble,
 447 while compensating downdrafts are established and closely wrap the rising bubble. This
 448 is a robust structure in convective elements and captures well the vertical fluxes of heat
 449 and moisture in convective systems (Gu et al., 2020). Meanwhile, a negative perturbation
 450 pressure is established below the maximum buoyancy level, while a positive perturbation
 451 pressure is established above it. As the buoyancy center is pushed upward as the
 452 bubble rises, the zero perturbation pressure contour line moves toward the bubble top,
 453 and negative P^\dagger dominates the majority of the bubble. A peak in negative P^\dagger develops
 454 at the center of the bubble, which results in a momentum source from the perturbation
 455 pressure gradient below this level and a momentum sink above it. The bottom panels
 456 in Figure 3 show the conditional average of the pressure gradient force and its decomposition
 457 into buoyancy and dynamic components. At the bottom and mid-levels of the
 458 bubble, $-\partial_z P_d^\dagger$ dominates; it is a momentum source in the lower part of the bubble and
 459 a sink near its top. The buoyancy component, $-\partial_z P_b^\dagger$, contributes primarily as a sink
 460 offsetting the buoyancy field.

461 During the early stages of the simulation (before 600 s), the 2D structure of the
 462 buoyancy and velocity fields resembles the trigonometric structure assumed in (6) and
 463 (7). Therefore, the single-normal mode assumption is a reasonable simplification. The

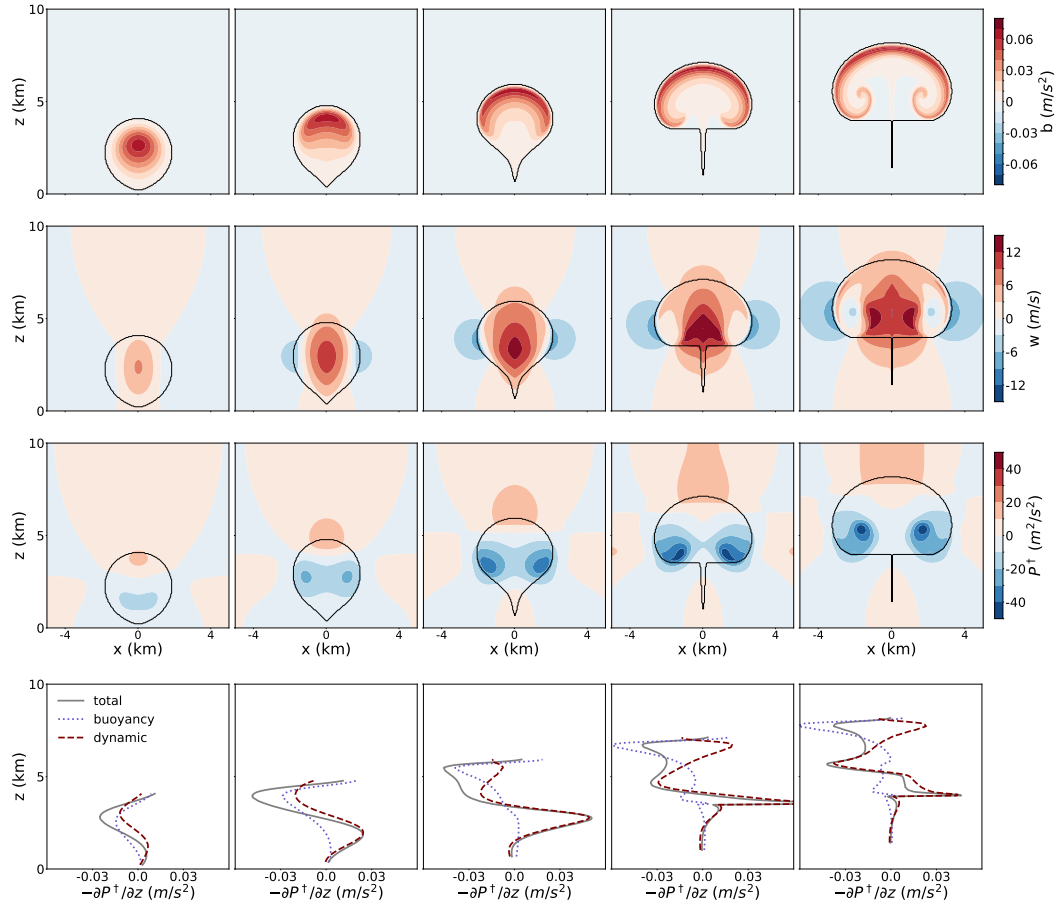


Figure 3. Snapshots of the rising bubble in 200-second intervals. The black contour in each contour plot traces the bubble boundary. From left to right are bubbles at 200, 400, 600, 800, and 1000 seconds into the simulation. The first 3 rows from top to bottom are buoyancy, vertical velocity, and perturbation pressure potential P^\dagger . The bottom row shows conditional averages of the perturbation pressure gradient force $-\partial_z P^\dagger$ and its decomposition into the buoyancy and dynamic components.

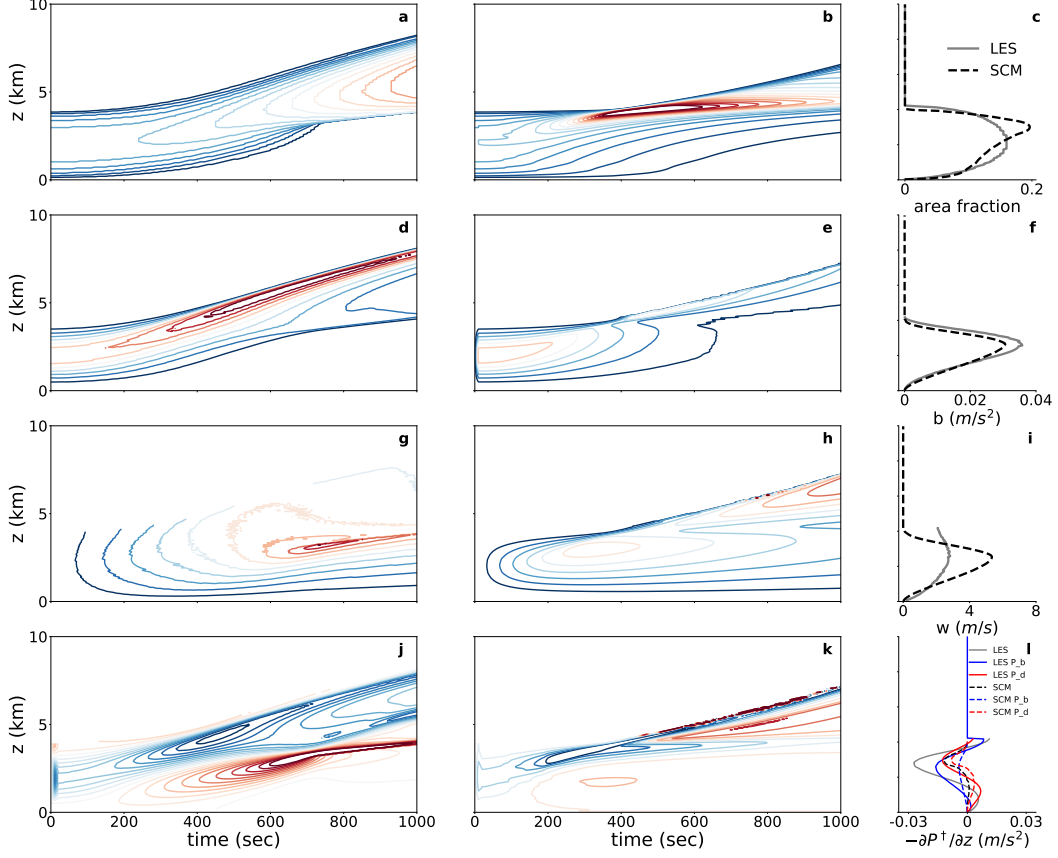


Figure 4. Comparison of bubble structures between LES and SCM simulations. (a) Time evolution of the bubble area fraction in LES. Contours from blue to red represent $[0.06, 0.08, \dots, 0.30]$. (b) Time evolution of the bubble area fraction in SCM. Contours from blue to red represent $[0.06, 0.08, \dots, 0.40]$. (c) Vertical profiles of area fraction for the 200-second step of the LES (solid) and SCM (dashed) simulations. (d) Time evolution of the bubble buoyancy in LES. Contours from blue to red represent $[0.005, 0.010, \dots, 0.045]$ m s^{-2} . (e) Time evolution of the bubble buoyancy in SCM. Contours from blue to red represent $[0.005, 0.010, \dots, 0.030]$ m s^{-2} . (f) As in (c) but for buoyancy. (g) Time evolution of the bubble vertical velocity in LES. Contours from blue to red represent $[1, 2, \dots, 9]$ m s^{-1} . (h) Time evolution of the bubble vertical velocity in SCM. Contours from blue to red represent $[1, 2, \dots, 8]$ m s^{-1} . (i) As in (c) but for vertical velocity. (j) Time evolution of the bubble $-\partial_z P^\dagger$ in LES. Contours from blue to red represent $[-0.05, -0.045, \dots, 0.045]$ m s^{-2} . (k) Time evolution of the bubble $-\partial_z P^\dagger$ in SCM. Contours from blue to red represent $[-0.01, -0.008, \dots, 0.01]$ m s^{-2} . (l) As in (c) but for $-\partial_z P^\dagger$ and its decomposition into the buoyancy and dynamic contributions.

464 perturbation pressure exhibits a dumbbell structure in the lower part of the bubble, which
 465 indicates the dynamic perturbation pressure associated with velocity plays an essential
 466 role at these levels. Toward the end of the simulation, when the bubble deforms, the flow
 467 inside the bubble deviates from the single-normal mode structure as the strong buoy-
 468 ancy is pushed to the bubble’s top while the maximum vertical velocity falls into the lower
 469 half of the bubble. However, a close investigation of the moist convective cases in the
 470 next subsection shows that individual bubbles in the convective system resemble the ris-
 471 ing bubble structures during the early stages, which validates the single-normal mode
 472 assumption made in the derivation.

473 The SCM with the extended EDMF parameterization and the pressure closure sim-
 474 ulates the time evolution of the rising thermal bubble well, with greater success at early
 475 stages, as shown in Figure 4. The time evolution shows a rising bubble that for the most
 476 part detaches from the surface and maintains a coherent buoyancy anomaly. As the bub-
 477 ble rises, the maximum buoyancy level in the SCM simulation shifts from the bubble’s
 478 center to its top, in agreement with the LES results. The area fraction shows a slightly
 479 sharper gradient at the top of the bubble at around 400 s. The SCM also roughly cap-
 480 tures the vertical velocity evolution in the LES. Throughout the simulation, the pertur-
 481 bation pressure gradient acts as important momentum source (see Figure 4j and 4k). How-
 482 ever, after 600 s in the simulation, the pressure gradient force’s contribution as momen-
 483 tum source stays at the lower half of the bubble in the LES but is pushed toward the
 484 bubble top in the SCM. This mismatch is a result of the discrepancies in w profiles in
 485 the later stages of the simulation, where the single-normal mode ansatz is no longer valid.

486 The last column of Figure 4 shows the profiles at 200 s simulation time, when the
 487 bubble has in a roughly symmetric structure and a single-normal mode is a reasonable
 488 assumption. The SCM reproduces the buoyancy profile from the LES, although it over-
 489 estimates the area fraction toward the bubble top and the vertical velocity throughout.
 490 In spite of these differences, the SCM produces a bubble that has many key features in
 491 the LES simulation. The $-(\partial P^\dagger/\partial z)_i$ profile in the SCM contributes to a slight momen-
 492 tum source in the lower half of the bubble and a momentum sink in the upper half, as
 493 expected from the LES diagnostics. However, the magnitude of the pressure gradient force
 494 in the SCM is smaller than in the LES. A decomposition into the dynamic and buoy-
 495 ancy perturbation pressure contributions shows that the buoyancy perturbation contri-
 496 bution is smaller than expected from LES. Considering the well-reproduced buoyancy
 497 profile, the underestimate of the buoyancy perturbation pressure gradient is mainly due
 498 to $\alpha_b = 0.14$ being too small. Since the bubble at 200 s has similar horizontal and ver-
 499 tical extents, the single-normal mode yields $\alpha_b \approx 0.5$. However, this constitutes too much
 500 inhibition and prevents the bubble from rising in the SCM setting. Despite the discrep-
 501 ancies in magnitude, the perturbation pressure gradient closure captures the primary physics
 502 of the perturbation pressure, i.e., the maintenance of a non-divergent flow. Overall, this
 503 demonstrates the capability of the EDMF framework with the pressure closure to sim-
 504 ulate a rising bubble.

505 5.2 Moist Convection

506 Thermal bubbles identified from the BOMEX and TRMM-LBA LES experiments
 507 demonstrate structures similar to the early stage of the rising thermal bubble experiment.
 508 Figure 5 shows the vertical velocity, buoyancy, perturbation pressure potential, and $-\partial_z P^\dagger$
 509 profiles for a composite of bubbles selected in the BOMEX and TRMM-LBA test cases.
 510 The buoyancy profiles resemble those of early-stage bubbles. The perturbation pressure
 511 fields show the clear pattern of low pressure in the middle and lower levels of the bub-
 512 ble and high pressure at the top. The dumbbell structure characterizing the later stages
 513 of the rising bubble experiment does not show up in the composite (averaged) fields in
 514 Figure 5; however, it does show up if one looks at individual bubbles instead of the com-
 515 posite. They are smoothed out when averaged over several bubbles with various hori-

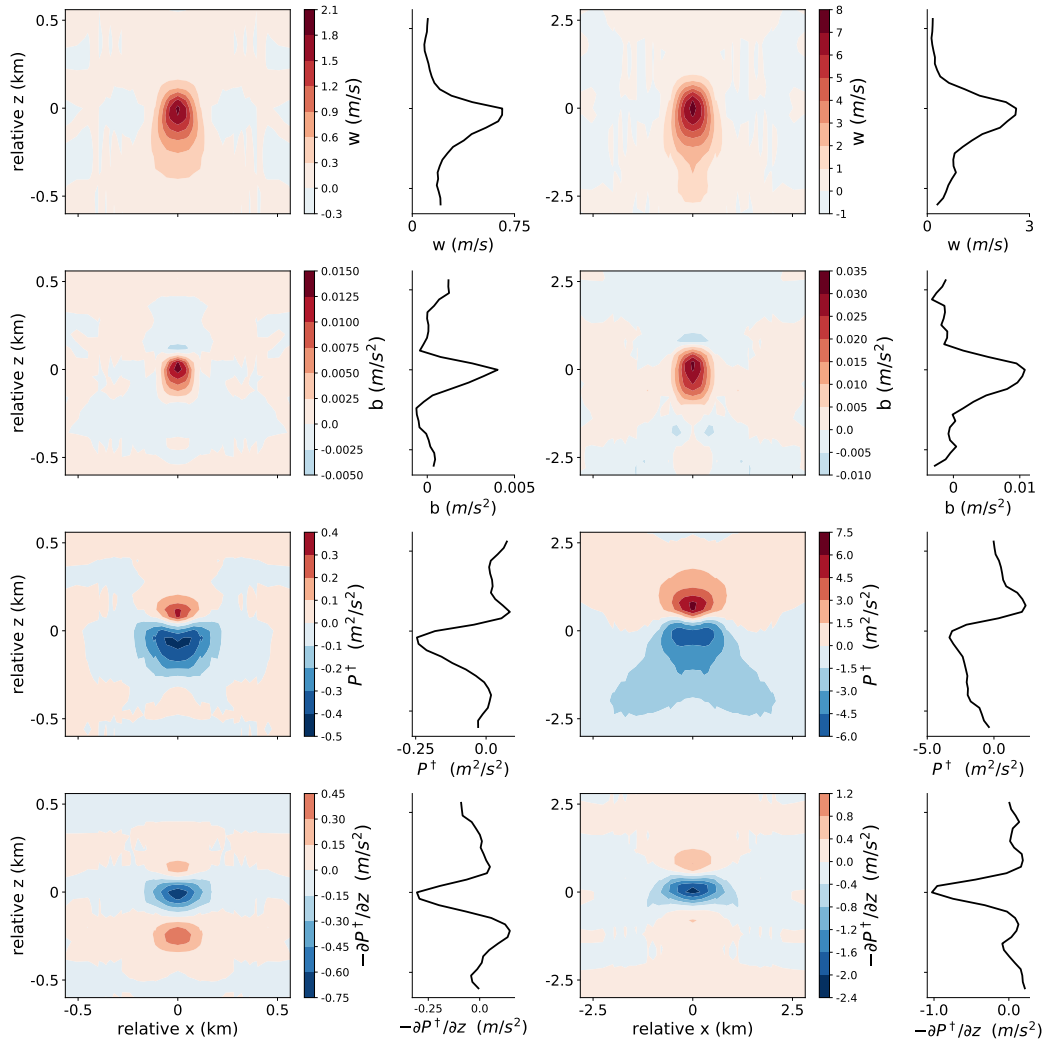


Figure 5. Average structures of bubble composites identified from LES simulations for BOMEX (left two columns) and TRMM-LBA (right two columns). Contour plots represent the azimuthally averaged structures of w , buoyancy, P^\dagger , and $-\partial_z P^\dagger$. The x and y axis in the contour plots represent the relative distances from the location of maximum vertical velocity. Column 2 (BOMEX) and 4 (TRMM-LBA) show the horizontal average of the bubble properties. Rows from top to bottom show vertical velocity, buoyancy, P^\dagger , and $-\partial_z P^\dagger$.

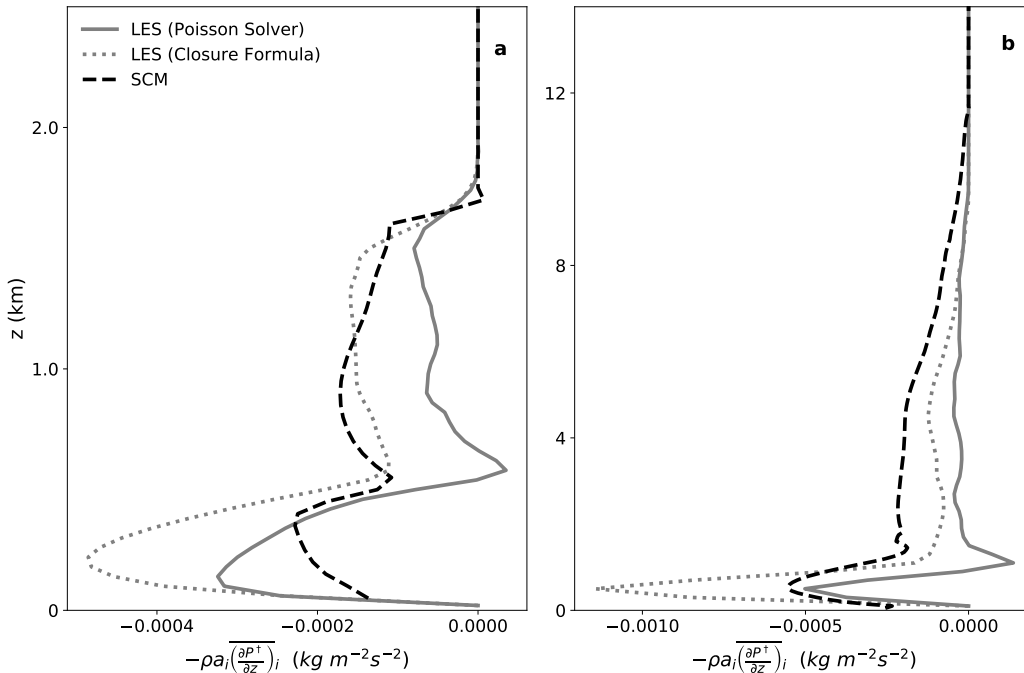


Figure 6. Comparison of $-\rho_i \overline{(\partial P^\dagger / \partial z)}_i$ between LES and SCM for BOMEX (left) and TRMM-LBA (right). Pressure in the LES is shown in the grey solid line; pressure diagnosed from LES using (34) is shown in the grey dotted line; pressure from SCM is shown in the black dashed line.

516 zontal and vertical extents. Averaged over many bubbles, the momentum source from
 517 $-\partial_z P^\dagger$ at the bottom of the bubble and the sink at the top remain similar to the struc-
 518 ture found in the rising bubble experiment.

519 The vertical velocity profiles show a much stronger asymmetry between upward and
 520 downward flow, compared to both the bubble experiment and the single-normal mode
 521 ansatz shown in Figure 1. This, however, is predicted by the single-normal mode solu-
 522 tion when averaging over thermals with different horizontal scales, as shown in Figure
 523 C1. Indeed, all fields in Figure 5 show a structure similar to that predicted by an en-
 524 semble of single-normal mode thermals. The resemblance between the composite of bub-
 525 bles from moist convection and the multi-mode ensemble (Figure C1) justifies the im-
 526 plementation of the proposed perturbation pressure closure in the EDMF framework.
 527 The analytical structure for the multi-thermal ensemble as shown in Figure C1 is also
 528 consistent with the idealized simulation results of Morrison (2016b).

529 Using the pressure closure described here, Cohen et al. (2020) demonstrate the ca-
 530 pability of the EDMF framework to represent dynamic and thermodynamic properties
 531 within the updrafts, as well as their first, second, and third moments. Here we focus on
 532 the performance of the pressure closure (34) in the BOMEX and TRMM-LBA cases through
 533 comparison between the LES and SCM simulations (Figure 6). Comparing the profiles
 534 for the vertical pressure gradient force in the SCM (dashed) with that diagnosed from
 535 (34) in LES (dotted), the SCM pressure closure captures the LES vertical profile well
 536 in the BOMEX case. For the TRMM-LBA case, the pressure gradient profile in the SCM
 537 represents a much larger momentum sink above the boundary layer compared to the LES.

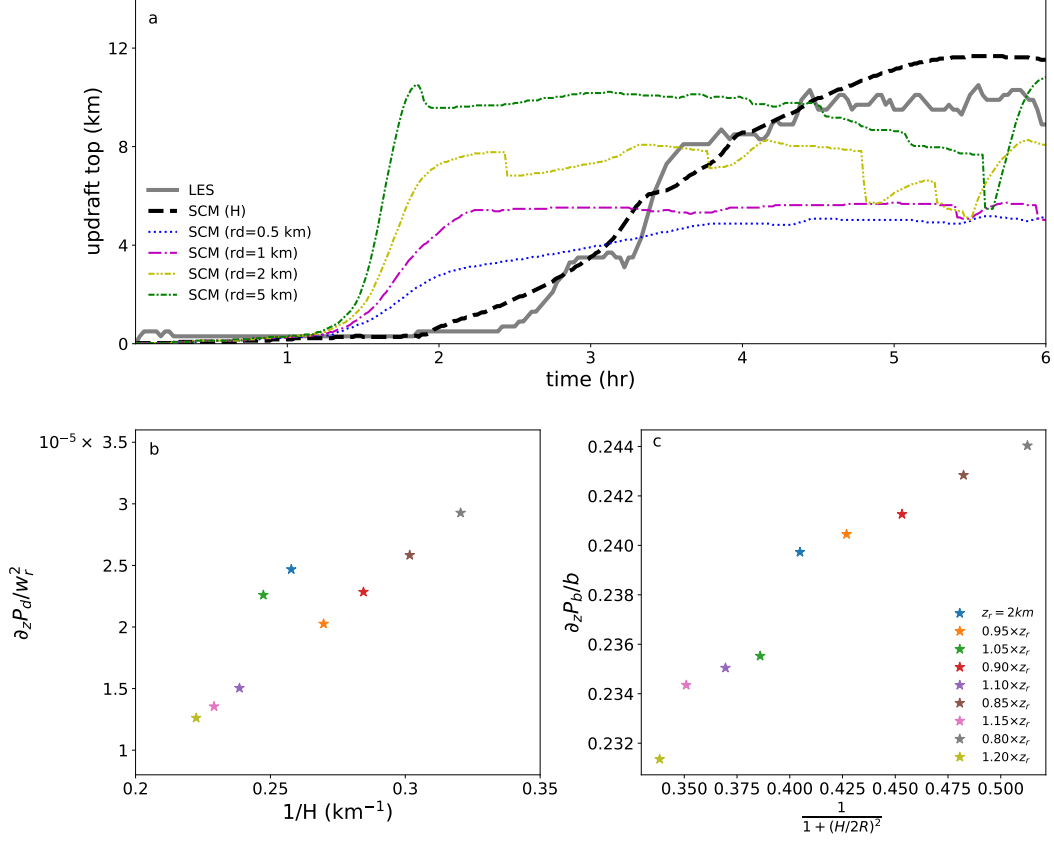


Figure 7. (a) Comparisons of the TRMM-LBA cloud top evolution between LES (grey solid line) and SCM simulations with different pressure drag closures. SCM results with updraft height as length scale, as given by (32), are shown in the black dashed line. SCM results with characteristic plume radius as length scale in the pressure drag, as given by (39), are shown in the colored dashed lines for different values of r_d . (b) $-\overline{(\partial P_d / \partial z)} / w_r^2$ versus $1/H$ where H is the vertical extent of the bubble in thermal bubble test case, the overbar represents a bubble average, and w_r is the ascent velocity of bubble measured at the bubble top. (c) $\overline{(\partial P_b / \partial z)} / b$ versus $(1 + (H/2R)^2)^{-1}$ where H and R are the vertical and horizontal extents of the bubble and b is the buoyancy.

538 This is primarily due to a discrepancy of the buoyancy profile between the SCM and LES
539 results, which leads to a larger sink from the buoyancy perturbation pressure component.

540 The EDMF framework represents the heat transport by the mass flux of the co-
541 herent updraft \bar{w}_i and the updraft buoyancy \bar{b}_i (neglecting the variance within each up-
542 draft) and the diffusive flux in the turbulent environment. Cohen et al. (2020) demon-
543 strate a well matched mass-flux profile and $\langle w^*\theta^* \rangle$ profile at the expense of accurate in-
544 dividual profiles of \bar{w}_i and \bar{b}_i . Comparing the pressure gradient profiles as diagnosed from
545 (34) (dotted) with that solved from the LES (solid), the former is about twice the mag-
546 nitude of the latter. This is due to a considerable drag effect ($\alpha_d = 10.0$). The large
547 drag effect is needed as a stabilization requirement (Weller & McIntyre, 2019). Unlike
548 for the buoyant bubble, the pressure gradient force for the bulk updrafts in BOMEX and
549 TRMM-LBA acts primarily as a momentum sink throughout the column, except at the
550 cloud base.

551 6 Discussion

An advantage of the current pressure closure manifests itself when examining the
diurnal cycle of deep convection in SCM simulations and LES. Simulating the diurnal
cycle is a major challenge for many parameterization schemes (Dai & Trenberth, 2004;
Holtzlag et al., 2013). Here we show the effect of the length scale used in the denomi-
nator of the pressure drag on the timing of deep convection. When using a fixed scale,
e.g., the updraft radius (Simpson & Wiggert, 1969; Tan et al., 2018), a trade-off arises
between improving the onset timing of convection and improving the cloud top height.
In Tan et al. (2018), the pressure drag term in the i -th subdomain was written as

$$-\left(\frac{\partial P_d^\dagger}{\partial z}\right)_i^* = -\alpha_d \frac{(\bar{w}_i^* - \bar{w}_0^*)|\bar{w}_i^* - \bar{w}_0^*|}{r_d \sqrt{a_i}}, \quad (39)$$

552 where $r_d = 500$ m is the typical distance between neighboring plumes in shallow con-
553 vection; thus, $r_d \sqrt{a_i}$ gives a characteristic plume radius. Our derivation indicates that
554 the drag effect scales with the vertical scale of the convective system. Figure 7 compares
555 the evolution of updraft tops in SCM and LES for the TRMM-LBA case. The SCM sim-
556 ulations have fixed coefficients $\alpha_b = 0.12$ and $\alpha_a = 0.1$. We compare the drag term
557 in closure (34) with expression (39) as in Tan et al. (2018). The value $r_d = 500$ m re-
558 produces shallow convection as in Tan et al. (2018), but it leads to too early onset and
559 too low updraft tops for the deep convective case. A simple increase in r_d results in a
560 universal decrease in the drag contribution and produces higher updraft tops. However,
561 this does not solve the problem of the onset timing. Physically, convection in the TRMM-
562 LBA case requires a large drag in the early stages, so that convection is not initiated too
563 early, and a gradually decreasing drag later, so that convection can grow high enough.
564 The height of the updraft top, which arises in the normal mode derivation above, is there-
565 fore a natural scale. The timing of the onset and the height of the updraft are both sub-
566 stantially improved when using the updraft height as a length scale. The same value of
567 α_d can be used for both shallow and deep convection.

568 The usefulness of the formulations derived from the single-normal mode approx-
569 imation is also evident in the rising bubble simulations. We performed a simple sensi-
570 tivity test by varying the vertical extent of the bubble (z_r) by factors ranging from 0.80
571 to 1.20, with intervals of 0.05. We computed mean thermal averages of all properties (e.g.,
572 the decomposed pressure gradient force, buoyancy, etc.) for the first 200 s of each sim-
573 ulations. Figure 7b and 7c show the H^{-1} scaling for the dynamic pressure gradient and
574 the $(1+(H/2R)^2)^{-1}$ for the virtual mass effect. This is consistent with previous anal-
575 yses of distinct thermals in convection (e.g., Romps and Charn (2015)).

576 We use the vertical scale H of the updraft as the length scale for the drag term.
577 In the buoyancy and the momentum advection terms, it appears in the aspect ratio, $H/(2R)$,

578 as a parameter characterizing the shape of the thermal. The parameters for the buoy-
 579 ancy and advection terms show a complicated dependency on the shape of the thermal:
 580 Changing from the 2D box pattern described by trigonometric functions to the 3D ax-
 581 isymmetric pattern described by Bessel functions, a scaling coefficient is needed in mod-
 582 ifying the aspect ratio in the formula. Thus, for a more realistic structure, we anticipate
 583 a more complicated modification will be needed. Instead of seeking the complicated de-
 584 pendencies on the dimensionless aspect ratio, we make the coefficient for buoyancy em-
 585 pirical and learn it from data.

586 The LES show that the perturbation pressure gradient force is a momentum source
 587 in the lower half of the bubble and near cloud base levels in moist convection, which en-
 588 sures the non-divergence property. This can be achieved only through the advection damp-
 589 ing term. However, its contribution in SCM settings is not as prominent as expected from
 590 LES diagnostics. In fact, the pair of parameters for the advection damping and the drag
 591 terms indicates their relative importance in the dynamic pressure gradient. In the moist
 592 convection experiments, the parameter combination $(\alpha_a, \alpha_d) = (0.1, 10.0)$ implies a neg-
 593 ligible contribution from the advection damping term. In the rising bubble experiment,
 594 by contrast, the advection damping contributes as an important source (Figure 3l) but
 595 with smaller magnitude compared with the LES results. In fact, the parameterization
 596 scheme contains multiple closure formula. With a proper choice of other parameters, one
 597 can manage to run the simulation successfully even without the advection damping term.
 598 Despite its small contribution as indicated by $\alpha_a = 0.1$, we retain this term in the clo-
 599 sure formula because it represents essential physics. The current parameter sets used here
 600 and in the other two companion EDMF papers (Cohen et al., 2020; Lopez-Gomez et al.,
 601 2020) are obtained through a sequential optimization processes with a limited set of cases.
 602 We expect to obtain better insights into the parameters with advanced parameter learn-
 603 ing techniques (Schneider et al., 2017; Cleary et al., 2021) and enlarged datasets (e.g.,
 604 generated as proposed in Shen et al. (2020)); this is reserved for future work.

605 There has been a continuous discussion of the plume-vs-thermal viewpoint for the
 606 representation of convective systems (Levine, 1959; Simpson et al., 1965; Yano, 2014; Mor-
 607 rison et al., 2020). Recent studies identify criteria (i.e., updraft width, environmental
 608 relative humidity, and available potential energy) for the transition between plume-like
 609 updrafts, thermal-like updrafts, and more complicated updraft structures consisting of
 610 successive thermals. It has been shown that the updraft structure impacts the patterns
 611 for the perturbation pressure (Morrison & Peters, 2018; Peters, 2016). Although the so-
 612 lution derived here is based on the diagnostic Poisson equation and follows from the single-
 613 normal mode ansatz for buoyancy and velocity, the updraft structure influences the spa-
 614 tial structure of the perturbation pressure. The EDMF scheme represents the SGS pro-
 615 cesses inside a grid cell by a turbulent environment and coherent updrafts. We view the
 616 updrafts as ensembles of discrete thermal bubbles with varying spatial scales and model
 617 their ensemble effect with the normal mode assumption.

618 7 Conclusion

619 We have derived an analytical formula for the perturbation pressure for convective
 620 systems under the assumption of a single-normal mode for individual thermals in a Boussi-
 621 nesq fluid. Large-eddy simulations show that the normal mode assumption is justified
 622 both for an idealized thermal bubble and for a composite average over thermal bubbles
 623 in moist convection. This perturbation pressure formula is essential to make the extended
 624 EDMF framework a unified parameterization for turbulence and convection across a range
 625 dynamical regimes. Specifically the pressure closure proposed here plays a key role in
 626 unifying both shallow and deep convection in a single model. Moreover, the extended
 627 EDMF framework with this pressure closure reproduces a dry rising bubble benchmark—
 628 an initial value problem rather than a boundary value problem—that can be consistently

629 simulated only in time dependent parameterizations (Tan et al., 2018; Thuburn et al.,
630 2018; Weller et al., 2020).

631 The pressure closure derived here consists of three components: a virtual mass term,
632 an advection damping term, and a drag term. The virtual mass and drag terms have been
633 proposed before (Simpson et al., 1965; de Roode et al., 2012; Siebesma et al., 2007; Tan
634 et al., 2018; Han & Bretherton, 2019; Davies-Jones, 2003; Doswell III & Markowski, 2004;
635 Jeevanjee & Romps, 2015); they represent momentum sinks. Additionally, the advec-
636 tion damping term has proven to be an important momentum source at the bottom of
637 convective systems (Schumann & Moeng, 1991; Jeevanjee & Romps, 2015; Morrison, 2016b).
638 Simplified expressions capturing it have been suggested before (Peters, 2016), but they
639 have not been tested in parameterization schemes. LES confirm the perturbation pres-
640 sure as an important momentum source for thermal bubbles as well as in shallow and
641 deep moist convection. The advection damping term is important for the dynamics of
642 transient convective bubbles, but less so in terms of bulk average properties. This indi-
643 cates that inclusion of the advection term may be important for simulating transient pro-
644 cesses. The drag term is consistent with previous LES diagnostics (Romps & Charn, 2015).
645 Thuburn et al. (2019) and Weller and McIntyre (2019) have additionally shown that it
646 is essential for numerical stability of EDMF-like schemes. The key modification in our
647 drag formula relative to other parameterizations is to replace the horizontal scale by the
648 vertical scale of the updraft. This enables an improved representation of the diurnal cy-
649 cle of deep convection.

650 An interesting distinction between a rising bubble and a coherent plume is that the
651 bubble gets detached from the surface at some point in time. As the discontinuous bot-
652 tom of the bubble rises, the perturbation pressure plays a key role as a momentum source
653 at the bottom. By contrast, a plume remains continuous from the surface upward and
654 does not have a strong momentum source from the perturbation pressure. Mass-flux mod-
655 els for clouds and convection are normally designed based on assuming plumes and have
656 difficulties simulating a rising bubble. The time-dependent parameterization scheme cir-
657 cumvents the distinction between plumes and bubbles (Yano, 2014) and can capture both
658 (Weller et al., 2020).

659 The extended EDMF scheme has the potential to unify SGS parameterizations of
660 turbulence and convection, given proper closures. The pressure closure presented in this
661 paper, the entrainment and detrainment closures presented in Cohen et al. (2020), and
662 the mixing length closure presented in Lopez-Gomez et al. (2020), allow this parame-
663 terization to represent a wide spectrum of different atmospheric boundary layers and con-
664 vective motions.

665 Appendix A Pressure Work for Environmental TKE

As assumed in Tan et al. (2018) and Lopez-Gomez et al. (2020), pressure does not
do work on the grid-mean TKE, but rather redistributes TKE between the subdomains,
that is,

$$-\left\langle \rho u^* \left(\frac{\partial P^\dagger}{\partial x} \right)^* + \rho v^* \left(\frac{\partial P^\dagger}{\partial y} \right)^* + \rho w^* \left(\frac{\partial P^\dagger}{\partial z} \right)^* \right\rangle = 0. \quad (\text{A1})$$

Following (22) and neglecting covariance terms $\overline{\phi'_i \psi'_i}$ except in the environment (i.e., $i = 0$), the grid-mean flux is decomposed into the ED and MF components

$$-\rho a_0 \left[w'_0 \left(\frac{\partial P^\dagger}{\partial z} \right)'_0 + u'_0 \left(\frac{\partial P^\dagger}{\partial x} \right)'_0 + v'_0 \left(\frac{\partial P^\dagger}{\partial y} \right)'_0 \right] - \sum_{i:i \geq 0} \rho a_i \bar{w}_i^* \left(\frac{\partial P^\dagger}{\partial z} \right)^*_i = 0. \quad (\text{A2})$$

Separating the environmental and plume contributions from the second term, moving them to the right-hand side and using the relationship $\sum_{i:i \geq 0} a_i \bar{\phi}_i^* = 0$ leads to

$$\begin{aligned}
 & -\rho a_0 \left[\overline{w'_0 \left(\frac{\partial P^\dagger}{\partial z} \right)' } + \overline{u'_0 \left(\frac{\partial P^\dagger}{\partial x} \right)' } + \overline{v'_0 \left(\frac{\partial P^\dagger}{\partial y} \right)' } \right] \\
 & = \rho a_0 \bar{w}_0^* \overline{\left(\frac{\partial P^\dagger}{\partial z} \right)' } + \sum_{i:i \geq 1} \rho a_i \bar{w}_i^* \overline{\left(\frac{\partial P^\dagger}{\partial z} \right)' }_i \\
 & = -\rho \bar{w}_0^* \sum_{i:i \geq 1} a_i \overline{\left(\frac{\partial P^\dagger}{\partial z} \right)' }_i + \sum_{i:i \geq 1} \rho a_i \bar{w}_i^* \overline{\left(\frac{\partial P^\dagger}{\partial z} \right)' }_i \\
 & = \sum_{i:i \geq 1} \rho a_i (\bar{w}_i^* - \bar{w}_0^*) \overline{\left(\frac{\partial P^\dagger}{\partial z} \right)' }_i. \quad (\text{A3})
 \end{aligned}$$

Appendix B Single-Normal Mode Solution for Axisymmetric Thermals

In the axisymmetric cylindrical coordinate system, the mass continuity equation is

$$\frac{\partial(ur)}{\partial r} + \frac{\partial(wr)}{\partial z} = 0, \quad (\text{B1})$$

where r and u denote the radial direction originating from the thermal's central axis and the radial velocity, z and w denote the vertical direction and vertical velocity.

The pressure Poisson equation in the axisymmetric cylindrical coordinate system is

$$\nabla_{r,z}^2 P^\dagger = \frac{\partial b}{\partial z} - \left[\left(\frac{\partial u}{\partial r} \right)^2 + \left(\frac{u}{r} \right)^2 + \left(\frac{\partial w}{\partial z} \right)^2 \right] - 2 \frac{\partial u}{\partial z} \frac{\partial w}{\partial r}. \quad (\text{B2})$$

Using the mass continuity equation, it simplifies to

$$\nabla_{r,z}^2 P^\dagger = \frac{\partial b}{\partial z} - 2 \left[\left(\frac{\partial w}{\partial z} \right)^2 + \frac{\partial u}{\partial z} \frac{\partial w}{\partial r} - \frac{u}{r} \frac{\partial u}{\partial r} \right], \quad (\text{B3})$$

where

$$\nabla_{r,z}^2 = \frac{1}{r} \frac{\partial}{\partial r} r \frac{\partial}{\partial r} + \frac{\partial^2}{\partial z^2}.$$

The perturbation pressure potential is decomposed into the sum of buoyancy and dynamic perturbation pressure, i.e., $P^\dagger = P_b + P_d$ such that

$$\begin{aligned}
 \nabla_{r,z}^2 P_b &= \frac{\partial b}{\partial z}, \\
 \nabla_{r,z}^2 P_d &= -2 \left[\left(\frac{\partial w}{\partial z} \right)^2 + \frac{\partial u}{\partial z} \frac{\partial w}{\partial r} - \frac{u}{r} \frac{\partial u}{\partial r} \right]. \quad (\text{B4})
 \end{aligned}$$

For an axisymmetric thermal bubble, a trigonometric basis is used for the vertical wave structure, as for the 2D derivation, while Bessel functions of the first kind $J_\alpha(\cdot)$ are used for the horizontal structure, to exploit eigenfunctions of the Laplacian operator (Holton, 1973). That is

$$\begin{aligned}
 b &= b_A \sin(mz) J_0(k_b r), \\
 w &= w_A \sin(mz) J_0(k_w r), \\
 u &= u_A \cos(mz) J_1(k_w r), \quad (\text{B5})
 \end{aligned}$$

where $m = \pi H^{-1}$ is the vertical wavenumber, and $k_b = 2.4R^{-1}$ ensures $k_b R$ is the first zero of the Bessel function, $J_0(k_b R) = 0$. The parameter R is the boundary for the thermal where buoyancy switches sign. Meanwhile, the flow satisfies a free-slip boundary condition at the thermal edges (where $J_1(k_w R) = 0$), which gives $k_w = 3.83R^{-1}$. Then, combining (B1) and (B5), with the identities of Bessel functions ($\frac{d}{dx}[xJ_1(x)] = xJ_0(x)$ and $\frac{d}{dx}J_0(x) = -J_1(x)$), gives

$$k_w u_A + m w_A = 0, \quad (\text{B6})$$

670 which is essential for simplifying the following derivation. The buoyancy and velocity structures of the axisymmetric thermal are shown in the bottom row of Figure 1.
671

672 B1 Buoyancy Perturbation Pressure

The buoyancy perturbation pressure satisfies

$$\nabla_{r,z}^2 P_b = m b_A \cos(mz) J_0(k_b r). \quad (\text{B7})$$

With the eigenfunction ansatz, this can be solved to give

$$P_b = -\frac{m}{m^2 + k_b^2} b_A \cos(mz) J_0(k_b r), \quad (\text{B8})$$

which gives the buoyancy perturbation pressure gradient as

$$\frac{\partial P_b}{\partial z} = \frac{m^2}{m^2 + k_b^2} b_A \sin(mz) J_0(k_b r) = \frac{1}{1 + \left(\frac{4.8}{\pi} \frac{H}{2R}\right)^2} b. \quad (\text{B9})$$

The buoyancy perturbation pressure gradient for a 3D thermal is

$$\left[1 + \left(\frac{4.8}{\pi} \frac{H}{2R} \right)^2 \right]^{-1} b, \quad (\text{B10})$$

673 which reaches the same formulation as the single-normal mode solution derived in Morrison
674 (2016b).

Similar to the 2D thermal, applying the conditional average over all the 3D thermals within the i -th subdomain yields

$$-\left(\frac{\partial P_b}{\partial z} \right)_i^* = \sum_{j=1}^N -\frac{1}{1 + \left(\frac{4.8}{\pi} \frac{H_j}{2R_j} \right)^2} \eta \bar{b}_i^* = -\eta \arctan \left(\frac{4.8}{\pi} \frac{H}{2R} \right) \bar{b}_i^*. \quad (\text{B11})$$

675 B2 Dynamic Perturbation Pressure

In cylindrical coordinates, the dynamic pressure includes a third term arising from the curvature of the coordinate system. The expansion of the dynamic perturbation pressure is done separately for each of the three terms, as follows:

$$\begin{aligned} \left(\frac{\partial w}{\partial z} \right)^2 &= (m w_A \cos(mz) J_0(k_w r))^2 \\ &= \frac{m^2}{2} w_A^2 (1 + \cos(2mz)) J_0^2(k_w r), \end{aligned} \quad (\text{B12})$$

$$\begin{aligned} \frac{\partial u}{\partial z} \frac{\partial w}{\partial r} &= [-m u_A \sin(mz) J_1(k_w r)] [w_A \sin(mz) (-k_w J_1(k_w r))] \\ &= m k_w u_A w_A \sin^2(mz) J_1^2(k_w r) \\ &= -\frac{m^2}{2} w_A^2 (1 - \cos(2mz)) J_1^2(k_w r), \end{aligned} \quad (\text{B13})$$

$$\begin{aligned}
 -\frac{u}{r} \frac{\partial u}{\partial r} &= -\left[\frac{u_A}{r} \cos(mz) J_1(k_w r) \right] \left[u_A \cos(mz) \left(k_w J_0(k_w r) - \frac{J_1(k_w r)}{r} \right) \right] \\
 &= -\frac{u_A^2}{2} (1 + \cos(2mz)) \left(\frac{k_w J_0(k_w r) J_1(k_w r)}{r} - \frac{J_1^2(k_w r)}{r^2} \right).
 \end{aligned} \tag{B14}$$

Using these expansions, the Poisson equation for dynamic perturbation pressure can be written as

$$\begin{aligned}
 \nabla_{r,z}^2 P_d &= -2 \left[\left(\frac{\partial w}{\partial z} \right)^2 + \frac{\partial u}{\partial z} \frac{\partial w}{\partial r} - \frac{u}{r} \frac{\partial u}{\partial r} \right] \\
 &= -m^2 w_A^2 (1 + \cos(2mz)) J_0^2(k_w r) + m^2 w_A^2 (1 - \cos(2mz)) J_1^2(k_w r) \\
 &\quad + u_A^2 (1 + \cos(2mz)) \left(\frac{k_w J_0(k_w r) J_1(k_w r)}{r} - \frac{J_1^2(k_w r)}{r^2} \right) \\
 &= -m^2 w_A^2 J_0^2(k_w r) - m^2 w_A^2 \cos(2mz) J_0^2(k_w r) + m^2 w_A^2 J_1^2(k_w r) - m^2 w_A^2 \cos(2mz) J_1^2(k_w r) \\
 &\quad + m^2 w_A^2 (1 + \cos(2mz)) \left[\frac{J_0(k_w r) J_1(k_w r)}{k_w r} - \frac{J_1^2(k_w r)}{k_w^2 r^2} \right].
 \end{aligned} \tag{B15}$$

Dividing both sides by $m^2 w_A^2$ and re-organizing the right-hand-side terms simplifies (B15) into

$$\begin{aligned}
 \nabla_{r,z}^2 \frac{P_d}{m^2 w_A^2} &= \underbrace{\left(-J_0^2(k_w r) + J_1^2(k_w r) + \underbrace{\left[\frac{J_0(k_w r) J_1(k_w r)}{k_w r} - \frac{J_1^2(k_w r)}{k_w^2 r^2} \right]}_{A'} \right)}_A \\
 &\quad + \underbrace{\cos(2mz) \left(-J_0^2(k_w r) - J_1^2(k_w r) + \left[\frac{J_0(k_w r) J_1(k_w r)}{k_w r} - \frac{J_1^2(k_w r)}{k_w^2 r^2} \right] \right)}_B.
 \end{aligned} \tag{B16}$$

676 Term A' comes from $\frac{1}{x} \frac{d}{dx} x \frac{d}{dx} J_1^2$. Similarly, $\frac{1}{x} \frac{d}{dx} x \frac{d}{dx}$ operating on J_0^2 and J_1^2 also gives
 677 J_0^2 and J_1^2 terms. However, J_0^2 and J_1^2 are not orthogonal functions. With the orthog-
 678 onality properties of Bessel functions of the same order, we will perform a Fourier-Bessel
 679 series expansion using the zeroth order Bessel functions as basis.

We expand term A in (B16) into Fourier-Bessel series as

$$g(x) = -J_0^2(x) + J_1^2(x) + \left[\frac{J_0(x) J_1(x)}{x} - \frac{J_1^2(x)}{x^2} \right] = \sum_{n=1}^{\infty} c_{n,g} J_0 \left(\frac{u_{0,n}}{b} x \right), \tag{B17}$$

680 where $x = k_w r$ and $b \approx 4.6317$ gives $g(b) = 0$; $u_{0,n}$ is the n -th root for $J_0(x) = 0$, and
 681 $c_{n,g}$ is the expansion coefficients calculated as

$$c_{n,g} = \frac{\int_0^b x g(x) J_0(u_{0,n} x/b) dx}{0.5 [b J_1(u_{0,n})]^2}. \tag{B18}$$

We then write term B in (B16) as

$$h(x) = -J_0^2(x) - J_1^2(x) + \left[\frac{J_0(x) J_1(x)}{x} - \frac{J_1^2(x)}{x^2} \right], \tag{B19}$$

and let

$$\tilde{h}(x) = h(x) - h(b), \tag{B20}$$

so that $\tilde{h}(b) = 0$, and we can expand $\tilde{h}(x)$ into Fourier-Bessel series in the same interval $[0, b]$ as for $g(x)$. The transformation in (B20) makes sure terms A and B are expanded to orthogonal basis in the same interval, that is

$$h(x) = h(b) + \tilde{h}(x) = h(b) + \sum_{n=1}^{\infty} c_{n,h} J_0\left(\frac{u_{0,n}}{b}x\right), \quad (\text{B21})$$

where $x = k_w r$, b , and $u_{0,n}$ are the same as in the $g(x)$ expansion, and $c_{n,f}$ is the coefficient for the Fourier-Bessel expansion for \tilde{h} ,

$$c_{n,h} = \frac{\int_0^b x \tilde{h}(x) J_0(u_{0,n}x/b) dx}{0.5[bJ_1(u_{0,n})]^2}. \quad (\text{B22})$$

Substituting A and B in (B16) by (B17) and (B21), the Fourier-Bessel expansion of the Poisson equation becomes

$$\begin{aligned} \nabla_{r,z}^2 \frac{P_d}{m^2 w_A^2} &= g(k_w r) + \cos(2mz)h(k_w r) \\ &= \sum_{n=1}^{\infty} c_{n,g} J_0\left(\frac{u_{0,n}}{b}k_w r\right) + \cos(2mz) \left[h(b) + \sum_{n=1}^{\infty} c_{n,h} J_0\left(\frac{u_{0,n}}{b}k_w r\right) \right]. \end{aligned} \quad (\text{B23})$$

Similar to the 2D derivation, we use an ansatz for $P_d/(m^2 w_A^2)$ of

$$\frac{P_d}{m^2 w_A^2} = \sum_{m=1}^{\infty} G_n J_0\left(\frac{u_{0,n}}{b}k_w r\right) + \cos(2mz) \sum_{m=1}^{\infty} H_n J_0\left(\frac{u_{0,n}}{b}k_w r\right) + X \cos(2mz) + Fz, \quad (\text{B24})$$

682 where G_n , H_n , and X need to be solved for by combining (B24) and (B23); F corresponds
683 to the drag coefficient and is obtained in the same way as the 2D case.

Taking the Laplacian of (B24) gives

$$\begin{aligned} \nabla_{r,z}^2 \frac{P_d}{m^2 w_A^2} &= \sum_{n=1}^{\infty} G_n \left[-\frac{u_{0,n}^2}{b^2} k_w^2 \right] J_0\left(\frac{u_{0,n}}{b}k_w r\right) + \cos(2mz) \left(\sum_{n=1}^{\infty} H_n \left[-\frac{u_{0,n}^2}{b^2} k_w^2 \right] J_0\left(\frac{u_{0,n}}{b}k_w r\right) \right) \\ &\quad - 4m^2 \cos(2mz) \sum_{m=1}^{\infty} H_n J_0\left(\frac{u_{0,n}}{b}k_w r\right) - 4m^2 X \cos(2mz). \end{aligned} \quad (\text{B25})$$

With the orthogonality between $J_0(\frac{u_{0,n}}{b}kr)$ and $J_0(\frac{u_{0,m}}{b}kr)$ $m \neq n$, the coefficients are obtained from

$$\begin{aligned} -\frac{u_{0,n}^2}{b^2} k_w^2 G_n &= c_{n,g}, \\ -\frac{u_{0,n}^2}{b^2} k_w^2 H_n - 4m^2 H_n &= c_{n,h}, \\ -4m^2 X &= h(b), \end{aligned} \quad (\text{B26})$$

as

$$\begin{aligned} G_n &= -\frac{b^2 c_{n,g}}{u_{0,n}^2 k_w^2}, \\ H_n &= -\frac{b^2 c_{n,h}}{u_{0,n}^2 k_w^2 + 4m^2 b^2}, \\ X &= -\frac{h(b)}{4m^2}, \end{aligned} \quad (\text{B27})$$

684 where $c_{n,g}$ and $c_{n,h}$ are obtained from the orthogonality of J_0 as in (B18) and (B22), and
685 $h(b) \approx -0.1394$.

The drag term F is obtained in the same way as the 2D case. We have

$$\int_0^{2\pi} d\theta \int_0^R \rho [P_d + \frac{1}{2}w^2]_{z=0}^{z=H} r dr = \frac{1}{2}\rho A c_d w_r^2 \quad (\text{B28})$$

where $A = \pi R^2$, and it solves

$$F = \frac{1}{2}c_d \frac{w_r^2}{H}. \quad (\text{B29})$$

We obtain the vertical gradient of dynamic perturbation pressure as

$$\begin{aligned} -\frac{\partial P_d}{\partial z} &= 2m^3 w_A^2 \sin(2mz) \sum_{m=1}^{\infty} H_n J_0\left(\frac{u_{0,n}}{b}kr\right) - \frac{h(b)}{2} m w_A^2 \sin(2mz) - F \\ &= 4m^2 w_A \sin(mz) \frac{d}{dz} [w_A \sin(mz)] \sum_{m=1}^{\infty} H_n J_0\left(\frac{u_{0,n}}{b}k_w r\right) - h(b) w_A \sin(mz) \frac{d}{dz} [w_A \sin(mz)] - F. \end{aligned} \quad (\text{B30})$$

To implement the perturbation pressure in the EDMF scheme, we perform a conditional average by applying

$$\sum_{j=1}^N \frac{1}{\pi R_j^2} \int_0^{2\pi} d\theta \int_0^{R_j} (\cdot) r dr$$

on (B30):

$$-\left(\frac{\partial P_d}{\partial z}\right)_i = \Gamma(m, k_w) \bar{w}_i \frac{d\bar{w}_i}{dz} - \alpha_d \frac{(\bar{w}_i - \bar{w}_0)|\bar{w}_i - \bar{w}_0|}{H_i}. \quad (\text{B31})$$

Here, the coefficient for the advective term,

$$\Gamma(k, m) = \sum_{j=1}^N \frac{1}{\pi R_j^2} \int_0^{2\pi} d\theta \int_0^{R_j} \left(4\gamma^2 m_j^2 \sum_{m=1}^{\infty} H_n J_0\left(\frac{u_{0,n}}{b}k_{w,j}r\right) \right) r dr - h(b),$$

686 has a complicated dependence on k and m and the Fourier-Bessel series coefficients H_n
687 from (B27).

688 The 3D analytical solution (B11) and (B31) demonstrates the same combination
689 of physical contributions to the perturbation pressure gradient force for the vertical mo-
690 mentum as the 2D solution. The parameters used in the scheme differ between 2D and
691 3D and are best learned empirically from data.

692 Appendix C A Multi-mode Representation for Thermals

693 The single-normal mode approximation aims to describe the pressure field inside
694 a thermal. In atmospheric flow, convection is driven by a multitude of short-lived suc-
695 cessive thermals that are represented in aggregate as towering updraft systems (e.g., Moser
696 and Lasher-Trapp (2017), Morrison et al. (2020)).

In the single-normal mode framework, the spatial structure of an aggregate of ther-
mal bubbles of different horizontal scales R_i and vertical scales H_i , centered at the cen-
troid of the thermal, is

$$\begin{aligned} b &= \sum_{i=1}^N b_{A,i} \cos(m_i z) \cos(k_{b,i} x) h_b(R_i, H_i), \\ w &= \sum_{i=1}^N w_{A,i} \cos(m_i z) \cos(k_{w,i} x) h_b(R_i, H_i). \end{aligned} \quad (\text{C1})$$

Here, h_b is defined as the product of Heaviside functions $h(\cdot)$

$$h_b(R_i, H_i) = h(R_i^2 - x^2) h(H_i^2 - 4z^2), \quad (\text{C2})$$

and ($x = 0, z = 0$) is the centroid of the thermal. Note that this frame of reference is different from the one used in (6) to facilitate the composite analysis of multi-thermals with respect to their centroids. Also note that h_b is zero outside the thermal bubble. This yields the buoyancy perturbation pressure

$$P_b = \sum_{i=1}^N \frac{m_i}{m_i^2 + k_{b,i}^2} b_{A,i} \sin(m_i z) \cos(k_{b,i} x) h_b(R_i, H_i), \quad (\text{C3})$$

and the dynamic perturbation pressure

$$P_d = \sum_{i=1}^N \left[-\frac{w_{A,i}^2}{4} \cos(2m_i z) + \frac{m_i^2 w_{A,i}^2}{4k_{w,i}^2} \cos(2k_{w,i} x) \right] h_b(R_i, H_i) + Fz. \quad (\text{C4})$$

Thus, the vertical gradients are

$$\begin{aligned} -\frac{\partial P_b}{\partial z} &= -\sum_{i=1}^N \frac{m_i^2}{m_i^2 + k_{b,i}^2} b_{A,i} \cos(m_i z) \cos(k_{b,i} x) h_b(R_i, H_i), \\ -\frac{\partial P_d}{\partial z} &= \sum_{i=1}^N w_{A,i} \cos(m_i z) \frac{d}{dz} [w_{A,i} \cos(m_i z)] h_b(R_i, H_i) - c_d \frac{w_r^2}{H}. \end{aligned} \quad (\text{C5})$$

697 In (C5), w_r and H represent the relative vertical velocity and height of the whole
 698 ensemble, respectively. Figure C1 sketches the buoyancy, velocity, and perturbation pres-
 699 sure patterns for an ensemble of 4 thermals with varying R_i but with the same $H_i =$
 700 H . The perturbation pressure structure here is consistent with the patterns shown in
 701 the idealized simulations in Morrison (2016b).

702 Acknowledgments

703 This research was made possible by the generosity of Eric and Wendy Schmidt by rec-
 704 ommendation of the Schmidt Futures program, by the Paul G. Allen Family Foundation,
 705 and the National Science Foundation (NSF, award AGS-1835860). We would like to thank
 706 the Resnick Sustainability Institute at Caltech for fellowship support. Parts of the re-
 707 search were carried out at the Jet Propulsion Laboratory, California Institute of Tech-
 708 nology, under a contract with the National Aeronautics and Space Administration and
 709 funded through the internal Research and Technology Development program. The Py-
 710 CLES code used to generate LES results is available at [climate-dynamics.org/software/](https://climate-dynamics.org/software/#pycles)
 711 [#pycles](https://climate-dynamics.org/software/#pycles). The SCM code is available at <https://doi.org/10.5281/zenodo.4291143>.

712 © 2021. California Institute of Technology. Government sponsorship acknowledged.

713 References

- 714 Bony, S., & Dufresne, J.-L. (2005). Marine boundary layer clouds at the heart of
 715 tropical cloud feedback uncertainties in climate models. *Geophysical Research*
 716 *Letters*, *32*(20). doi: <https://doi.org/10.1029/2005GL023851>
- 717 Bony, S., Stevens, B., Frierson, D. M., Jakob, C., Kageyama, M., Pincus, R., . . .
 718 others (2015). Clouds, circulation and climate sensitivity. *Nature Geoscience*,
 719 *8*(4), 261–268. doi: 0.1038/ngeo2398
- 720 Bretherton, C. S., & Park, S. (2009). A new moist turbulence parameterization in
 721 the community atmosphere model. *Journal of Climate*, *22*(12), 3422–3448. doi:
 722 <https://doi.org/10.1175/2008JCLI2556.1>
- 723 Brient, F., & Schneider, T. (2016). Constraints on climate sensitivity from space-
 724 based measurements of low-cloud reflection. *Journal of Climate*, *29*(16), 5821–
 725 5835. doi: <https://doi.org/10.1175/JCLI-D-15-0897.1>

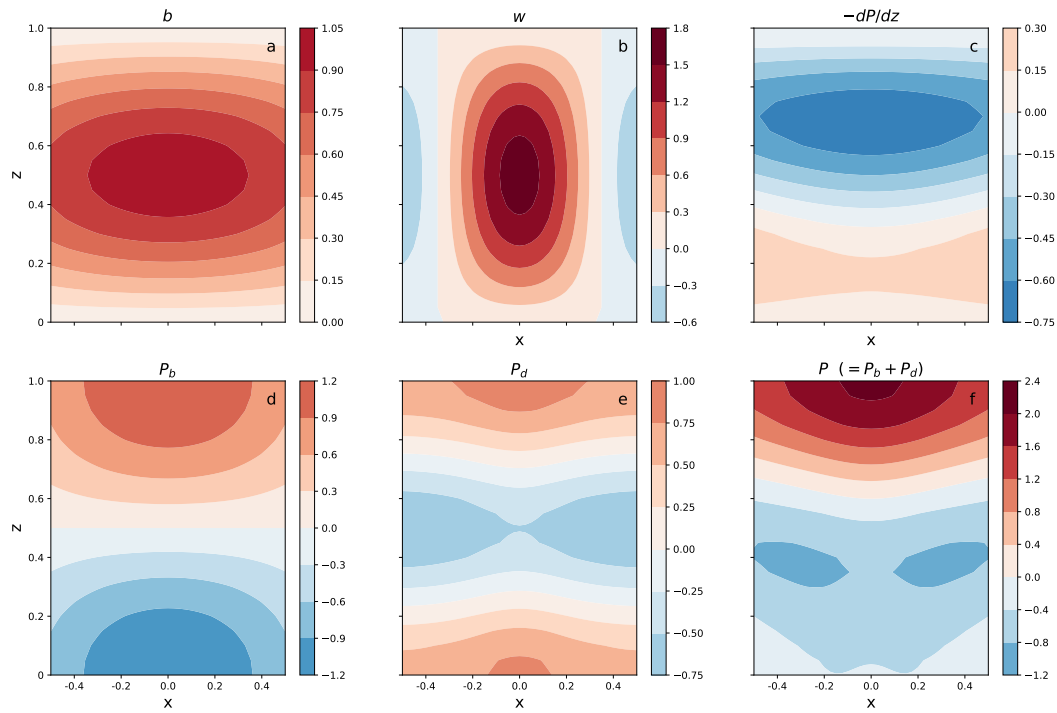


Figure C1. The structures for buoyancy (a), vertical velocity (b), vertical pressure gradient force (c), P_b (d), P_d (e), and perturbation pressure ($P_b + P_d$) (f) for an ensemble of 4 thermals. The thermal is created by specifying dimensionless $H = 1$ and varying horizontal scale $[0.2, 0.333, 0.467, 0.6]$.

- 726 Bryan, G. H., & Fritsch, J. M. (2002). A benchmark simulation for moist nonhydro-
727 static numerical models. *Monthly Weather Review*, *130*(12), 2917–2928. doi:
728 [https://doi.org/10.1175/1520-0493\(2002\)130<2917:ABSFMN>2.0.CO;2](https://doi.org/10.1175/1520-0493(2002)130<2917:ABSFMN>2.0.CO;2)
- 729 Caldwell, P. M., Zelinka, M. D., & Klein, S. A. (2018). Evaluating emergent con-
730 straints on equilibrium climate sensitivity. *Journal of Climate*, *31*(10), 3921–
731 3942. doi: 10.1175/JCLI-D-17-0631.1
- 732 Ceppi, P., Brient, F., Zelinka, M. D., & Hartmann, D. L. (2017). Cloud feedback
733 mechanisms and their representation in global climate models. *Wiley Interdis-*
734 *ciplinary Reviews: Climate Change*, *8*(4), e465. doi: 10.1002/wcc.465
- 735 Cleary, E., Garbuno-Inigo, A., Lan, S., Schneider, T., & Stuart, A. M. (2021). Cali-
736 brate, emulate, sample. *J. Comp. Phys.*, *424*, 109716.
- 737 Cohen, Y., Lopez-Gomez, I., Jaruga, A., He, J., Kaul, C. M., & Schneider, T.
738 (2020). Unified entrainment and detrainment closures for extended eddy-
739 diffusivity mass-flux schemes. *Journal of Advances in Modeling Earth Systems*,
740 *12*(9), e2020MS002162. doi: 10.1029/2020MS002162
- 741 Couvreux, F., Hourdin, F., & Rio, C. (2010). Resolved versus parametrized
742 boundary-layer plumes. part i: A parametrization-oriented conditional sam-
743 pling in large-eddy simulations. *Boundary-layer meteorology*, *134*(3), 441–458.
744 doi: 10.1007/s10546-009-9456-5
- 745 Dai, A., & Trenberth, K. E. (2004). The diurnal cycle and its depiction in the
746 community climate system model. *Journal of Climate*, *17*(5), 930–951. doi:
747 [https://doi.org/10.1175/1520-0442\(2004\)017<0930:TDCRID>2.0.CO;2](https://doi.org/10.1175/1520-0442(2004)017<0930:TDCRID>2.0.CO;2)
- 748 Davies-Jones, R. (2003). An expression for effective buoyancy in surroundings
749 with horizontal density gradients. *Journal of the atmospheric sciences*,
750 *60*(23), 2922–2925. doi: [https://doi.org/10.1175/1520-0469\(2003\)060<2922:](https://doi.org/10.1175/1520-0469(2003)060<2922:AEFEFI>2.0.CO;2)
751 [AEFEFI>2.0.CO;2](https://doi.org/10.1175/1520-0469(2003)060<2922:AEFEFI>2.0.CO;2)
- 752 de Roode, S. R., Siebesma, A. P., Jonker, H. J. J., & de Voogd, Y. (2012). Parame-
753 terization of the vertical velocity equation for shallow cumulus clouds. *Monthly*
754 *Weather Review*, *140*(8), 2424–2436. doi: 10.1175/MWR-D-11-00277.1
- 755 Doswell III, C. A., & Markowski, P. M. (2004). Is buoyancy a relative quantity?
756 *Monthly weather review*, *132*(4), 853–863. doi: [https://doi.org/10.1175/1520-](https://doi.org/10.1175/1520-0493(2004)132<0853:IBARQ>2.0.CO;2)
757 [0493\(2004\)132<0853:IBARQ>2.0.CO;2](https://doi.org/10.1175/1520-0493(2004)132<0853:IBARQ>2.0.CO;2)
- 758 Giordani, H., Bourdallé-Badie, R., & Madec, G. (2020). An eddy-diffusivity mass-
759 flux parameterization for modelling oceanic convection. *Journal of Advances*
760 *in Modeling Earth Systems*, e2020MS002078. doi: [https://doi.org/10.1029/](https://doi.org/10.1029/2020MS002078)
761 [2020MS002078](https://doi.org/10.1029/2020MS002078)
- 762 Golaz, J.-C., Larson, V. E., & Cotton, W. R. (2002a). A pdf-based model for bound-
763 ary layer clouds. part ii: Model results. *Journal of the Atmospheric Sciences*,
764 *59*(24), 3552–3571. doi: [https://doi.org/10.1175/1520-0469\(2002\)059<3552:](https://doi.org/10.1175/1520-0469(2002)059<3552:APBMFB>2.0.CO;2)
765 [APBMFB>2.0.CO;2](https://doi.org/10.1175/1520-0469(2002)059<3552:APBMFB>2.0.CO;2)
- 766 Golaz, J.-C., Larson, V. E., & Cotton, W. R. (2002b). A pdf-based model for
767 boundary layer clouds. part i: Method and model description. *Journal of*
768 *the Atmospheric Sciences*, *59*(24), 3540–3551. doi: [https://doi.org/10.1175/](https://doi.org/10.1175/1520-0469(2002)059<3540:APBMFB>2.0.CO;2)
769 [1520-0469\(2002\)059<3540:APBMFB>2.0.CO;2](https://doi.org/10.1175/1520-0469(2002)059<3540:APBMFB>2.0.CO;2)
- 770 Grabowski, W., Bechtold, P., Cheng, A., Forbes, R., Halliwell, C., Khairoutdinov,
771 M., . . . et al. (2006). Daytime convective development over land: A model
772 intercomparison based on lba observations. *Quarterly Journal of the Royal*
773 *Meteorological Society*, *132*(615), 317–344. doi: doi.org/10.1256/qj.04.147
- 774 Gu, J.-F., Plant, R. S., Holloway, C. E., Jones, T. R., Stirling, A., Clark, P. A., . . .
775 Webb, T. L. (2020). Evaluation of the bulk mass flux formulation using large-
776 eddy simulations. *Journal of the Atmospheric Sciences*, *77*(6), 2115–2137. doi:
777 <https://doi.org/10.1175/JAS-D-19-0224.1>
- 778 Han, J., & Bretherton, C. S. (2019). Tke-based moist eddy-diffusivity mass-flux
779 (edmf) parameterization for vertical turbulent mixing. *Weather and Forecast-*
780 *ing*, *34*(4), 869–886. doi: 10.1175/WAF-D-18-0146.1

- 781 Heinze, R., Mironov, D., & Raasch, S. (2015). Second-moment budgets in cloud
782 topped boundary layers: A large-eddy simulation study. *Journal of Advances*
783 *in Modeling Earth Systems*, 7(2), 510–536. doi: 10.1002/2014MS000376
- 784 Hernandez-Deckers, D., & Sherwood, S. C. (2016). A numerical investigation of cu-
785 mulus thermals. *Journal of the Atmospheric Sciences*, 73(10), 4117–4136.
- 786 Holland, J. Z., & Rasmusson, E. M. (1973). Measurements of the atmospheric
787 mass, energy, and momentum budgets over a 500-kilometer square of trop-
788 ical ocean. *Monthly Weather Review*, 101(1), 44–57. doi: 10.1175/
789 1520-0493(1973)101<0044:MOTAME>2.3.CO;2
- 790 Holton, J. R. (1973). A one-dimensional cumulus model including pressure per-
791 turbations. *Monthly Weather Review*, 101(3), 201–205. doi: 10.1175/1520-
792 -0493(1973)101<0201:AOCMIP>2.3.CO;2
- 793 Holtslag, A., Svensson, G., Baas, P., Basu, S., Beare, B., Beljaars, A., . . . others
794 (2013). Stable atmospheric boundary layers and diurnal cycles: challenges for
795 weather and climate models. *Bulletin of the American Meteorological Society*,
796 94(11), 1691–1706. doi: <https://doi.org/10.1175/BAMS-D-11-00187.1>
- 797 Jeevanjee, N., & Romps, D. M. (2015). Effective buoyancy, inertial pressure, and the
798 mechanical generation of boundary layer mass flux by cold pools. *Journal of*
799 *the Atmospheric Sciences*, 72(8), 3199–3213. doi: 10.1175/JAS-D-14-0349.1
- 800 Jeevanjee, N., & Romps, D. M. (2016). Effective buoyancy at the surface and aloft.
801 *Quarterly Journal of the Royal Meteorological Society*, 142(695), 811–820. doi:
802 <https://doi.org/10.1002/qj.2683>
- 803 Lappen, C.-L., & Randall, D. A. (2001a). Toward a unified parameterization
804 of the boundary layer and moist convection. part i: A new type of mass-
805 flux model. *Journal of the Atmospheric Sciences*, 58(15), 2021–2036. doi:
806 [https://doi.org/10.1175/1520-0469\(2001\)058<2021:TAUPOT>2.0.CO;2](https://doi.org/10.1175/1520-0469(2001)058<2021:TAUPOT>2.0.CO;2)
- 807 Lappen, C.-L., & Randall, D. A. (2001b). Toward a unified parameterization of the
808 boundary layer and moist convection. part iii: Simulations of clear and cloudy
809 convection. *Journal of the Atmospheric Sciences*, 58(15), 2052–2072. doi:
810 [https://doi.org/10.1175/1520-0469\(2001\)058<2052:TAUPOT>2.0.CO;2](https://doi.org/10.1175/1520-0469(2001)058<2052:TAUPOT>2.0.CO;2)
- 811 Lappen, C.-L., & Randall, D. A. (2001c). Toward a unified parameterization of
812 the boundary layer and moist convection. part ii: Lateral mass exchanges and
813 subplume-scale fluxes. *Journal of the Atmospheric Sciences*, 58(15), 2037–2051.
814 doi: [https://doi.org/10.1175/1520-0469\(2001\)058<2037:TAUPOT>2.0.CO;2](https://doi.org/10.1175/1520-0469(2001)058<2037:TAUPOT>2.0.CO;2)
- 815 Lappen, C.-L., & Randall, D. A. (2006). Parameterization of pressure perturba-
816 tions in a pbl mass-flux model. *Journal of the atmospheric sciences*, 63(7),
817 1726–1751. doi: <https://doi.org/10.1175/JAS3722.1>
- 818 Larson, V. E., & Golaz, J.-C. (2005). Using probability density functions to de-
819 rive consistent closure relationships among higher-order moments. *Monthly*
820 *Weather Review*, 133(4), 1023–1042. doi: 10.1175/MWR2902.1
- 821 Leger, J., Lafore, J.-P., Piriou, J.-M., & Gu er emy, J.-F. (2019). A simple model of
822 convective drafts accounting for the perturbation pressure term. *Journal of the*
823 *Atmospheric Sciences*, 76(10), 3129–3149. doi: 10.1175/JAS-D-18-0281.1
- 824 Levine, J. (1959). Spherical vortex theory of bubble-like motion in cumulus clouds.
825 *Journal of Atmospheric Sciences*, 16(6), 653–662.
- 826 Liu, L., Zhu, J., & Wu, J. (2015). Lift and drag in two-dimensional steady viscous
827 and compressible flow. *Journal of Fluid Mechanics*, 784, 304.
- 828 Lopez-Gomez, I., Cohen, Y., He, J., Jaruga, A., & Schneider, T. (2020). A gen-
829 eralized mixing length closure for eddy-diffusivity mass-flux schemes of tur-
830 bulence and convection. *Journal of Advances in Modeling Earth Systems*,
831 e2020MS002161. doi: 10.1029/2020MS002161
- 832 Morrison, H. (2016a). Impacts of updraft size and dimensionality on the perturba-
833 tion pressure and vertical velocity in cumulus convection. part ii: Comparison
834 of theoretical and numerical solutions and fully dynamical simulations. *Journal*
835 *of the Atmospheric Sciences*, 73(4), 1455–1480.

- 836 Morrison, H. (2016b). Impacts of updraft size and dimensionality on the pertur-
 837 bation pressure and vertical velocity in cumulus convection. part i: Simple,
 838 generalized analytic solutions. *Journal of the Atmospheric Sciences*, *73*(4),
 839 1441-1454. doi: 10.1175/JAS-D-15-0040.1
- 840 Morrison, H., & Peters, J. M. (2018). Theoretical expressions for the ascent rate
 841 of moist deep convective thermals. *Journal of the Atmospheric Sciences*, *75*(5),
 842 1699-1719.
- 843 Morrison, H., Peters, J. M., & Sherwood, S. C. (2021). Comparing growth rates of
 844 simulated moist and dry convective thermals. *Journal of the Atmospheric Sci-*
 845 *ences*, *78*(3), 797-816.
- 846 Morrison, H., Peters, J. M., Varble, A. C., Hannah, W. M., & Giangrande, S. E.
 847 (2020). Thermal chains and entrainment in cumulus updrafts. part i: Theoret-
 848 ical description. *Journal of the Atmospheric Sciences*, *77*(11), 3637-3660.
- 849 Moser, D. H., & Lasher-Trapp, S. (2017). The influence of successive thermals on en-
 850 trainment and dilution in a simulated cumulus congestus. *Journal of the Atmo-*
 851 *spheric Sciences*, *74*(2), 375-392.
- 852 Murphy, J. M., Sexton, D. M., Barnett, D. N., Jones, G. S., Webb, M. J., Collins,
 853 M., & Stainforth, D. A. (2004). Quantification of modelling uncertainties in a
 854 large ensemble of climate change simulations. *Nature*, *430*(7001), 768-772. doi:
 855 10.1038/nature02771
- 856 Park, S. (2014a). A unified convection scheme (unicon). part i: Formulation. *Journal*
 857 *of the Atmospheric Sciences*, *71*(11), 3902-3930. doi: [https://doi.org/10.1175/
 858 JAS-D-13-0233.1](https://doi.org/10.1175/JAS-D-13-0233.1)
- 859 Park, S. (2014b). A unified convection scheme (unicon). part ii: Simulation. *Journal*
 860 *of the Atmospheric Sciences*, *71*(11), 3931-3973. doi: [https://doi.org/10.1175/
 861 JAS-D-13-0234.1](https://doi.org/10.1175/JAS-D-13-0234.1)
- 862 Peters, J. M. (2016). The impact of effective buoyancy and dynamic pressure forc-
 863 ing on vertical velocities within two-dimensional updrafts. *Journal of the At-*
 864 *mospheric Sciences*, *73*(11), 4531-4551. doi: 10.1175/JAS-D-16-0016.1
- 865 Peters, J. M., Morrison, H., Varble, A. C., Hannah, W. M., & Giangrande, S. E.
 866 (2020). Thermal chains and entrainment in cumulus updrafts. part ii: Analysis
 867 of idealized simulations. *Journal of Atmospheric Sciences*, *77*(11), 3661-3681.
- 868 Pressel, K. G., Kaul, C. M., Schneider, T., Tan, Z., & Mishra, S. (2015). Large-
 869 eddy simulation in an anelastic framework with closed water and entropy
 870 balances. *Journal of Advances in Modeling Earth Systems*, *7*(3), 1425-1456.
 871 doi: <https://doi.org/10.1002/2015MS000496>
- 872 Romps, D. M., & Charn, A. B. (2015). Sticky thermals: Evidence for a dominant
 873 balance between buoyancy and drag in cloud updrafts. *Journal of the Atmo-*
 874 *spheric Sciences*, *72*(8), 2890-2901. doi: 10.1175/JAS-D-15-0042.1
- 875 Sánchez, O., Raymond, D. J., Libersky, L., & Petschek, A. G. (1989). The de-
 876 velopment of thermals from rest. *Journal of the atmospheric sciences*,
 877 *46*(14), 2280-2292. doi: [https://doi.org/10.1175/1520-0469\(1989\)046<2280:
 878 TDOTFR>2.0.CO;2](https://doi.org/10.1175/1520-0469(1989)046<2280:TDOTFR>2.0.CO;2)
- 879 Schneider, T., Teixeira, J., Bretherton, C. S., Brient, F., Pressel, K. G., Schär, C., &
 880 Siebesma, A. P. (2017). Climate goals and computing the future of clouds. *Na-*
 881 *ture Climate Change*, *7*(1), 3-5. doi: <https://doi.org/10.1038/nclimate3190>
- 882 Schumann, U., & Moeng, C.-H. (1991). Plume budgets in clear and cloudy convective
 883 boundary layers. *Journal of the Atmospheric Sciences*, *48*(15), 1758-1770.
 884 doi: 10.1175/1520-0469(1991)048<1758:PBICAC>2.0.CO;2
- 885 Shen, Z., Pressel, K. G., Tan, Z., & Schneider, T. (2020). Statistically steady state
 886 large-eddy simulations forced by an idealized gcm: 1. forcing framework and
 887 simulation characteristics. *Journal of Advances in Modeling Earth Systems*,
 888 *12*(2), e2019MS001814.
- 889 Sherwood, S. C., Hernández-Deckers, D., Colin, M., & Robinson, F. (2013). Slippery
 890 thermals and the cumulus entrainment paradox. *Journal of the Atmospheric*

- 891 *Sciences*, 70(8), 2426–2442.
- 892 Siebesma, A. P., Bretherton, C. S., Brown, A., Chlond, A., Cuxart, J., Duynkerke,
893 P. G., . . . others (2003). A large eddy simulation intercomparison study of
894 shallow cumulus convection. *Journal of the Atmospheric Sciences*, 60(10),
895 1201–1219.
- 896 Siebesma, A. P., Soares, P. M. M., & Teixeira, J. (2007). A combined eddy-
897 diffusivity mass-flux approach for the convective boundary layer. *Journal*
898 *of the Atmospheric Sciences*, 64(4), 1230–1248. doi: 10.1175/JAS3888.1
- 899 Simpson, J., Simpson, R. H., Andrews, D. A., & Eaton, M. A. (1965). Experimen-
900 tal cumulus dynamics. *Reviews of Geophysics*, 3(3), 387–431. doi: 10.1029/
901 RG003i003p00387
- 902 Simpson, J., & Wiggert, V. (1969). Models of precipitating cumulus tow-
903 ers. *Mon. Wea. Rev.*, 97(7), 471–489. doi: [https://doi.org/10.1175/
904 1520-0493\(1969\)097\(0471:MOPCT\)2.3.CO;2](https://doi.org/10.1175/1520-0493(1969)097(0471:MOPCT)2.3.CO;2)
- 905 Soares, P. M. M., Miranda, P. M. A., Siebesma, A. P., & Teixeira, J. (2004). An
906 eddy-diffusivity/mass-flux parametrization for dry and shallow cumulus con-
907 vection. *Quarterly Journal of the Royal Meteorological Society*, 130(604),
908 3365–3383. doi: 10.1256/qj.03.223
- 909 Suselj, K., Kurowski, M. J., & Teixeira, J. (2019). On the factors controlling the de-
910 velopment of shallow convection in eddy-diffusivity/mass-flux models. *Journal*
911 *of the Atmospheric Sciences*, 76(2), 433–456. doi: 10.1175/JAS-D-18-0121.1
- 912 Tan, Z., Kaul, C. M., Pressel, K. G., Cohen, Y., Schneider, T., & Teixeira, J. (2018).
913 An extended eddy-diffusivity mass-flux scheme for unified representation of
914 subgrid-scale turbulence and convection. *Journal of Advances in Modeling*
915 *Earth Systems*, 10(3), 770–800. doi: 10.1002/2017MS001162
- 916 Tarshish, N., Jeevanjee, N., & Lecoanet, D. (2018). Buoyant motion of a turbulent
917 thermal. *Journal of the Atmospheric Sciences*, 75(9), 3233–3244. doi: 10.1175/
918 JAS-D-17-0371.1
- 919 Teixeira, J., Cardoso, S., Bonazzola, M., Cole, J., DelGenio, A., DeMott, C., . . . oth-
920 ers (2011). Tropical and subtropical cloud transitions in weather and climate
921 prediction models: The gcss/wgne pacific cross-section intercomparison (gpci).
922 *Journal of Climate*, 24(20), 5223–5256. doi: 10.1175/2011JCLI3672.1
- 923 Thuburn, J., Efstathiou, G. A., & Beare, R. J. (2019). A two-fluid single-column
924 model of the dry, shear-free, convective boundary layer. *Quarterly Journal of*
925 *the Royal Meteorological Society*, 145(721), 1535–1550. doi: 10.1002/qj.3510
- 926 Thuburn, J., Weller, H., Vallis, G. K., Beare, R. J., & Whittall, M. (2018). A
927 framework for convection and boundary layer parameterization derived from
928 conditional filtering. *Journal of the Atmospheric Sciences*, 75(3), 965–981. doi:
929 10.1175/JAS-D-17-0130.1
- 930 Webb, M. J., Lambert, F. H., & Gregory, J. M. (2013). Origins of differences in
931 climate sensitivity, forcing and feedback in climate models. *Climate Dynamics*,
932 40(3–4), 677–707. doi: 10.1007/s00382-012-1336-x
- 933 Weller, H., McIntyre, W., & Shipley, D. (2020). Multifluids for representing
934 subgrid-scale convection. *Journal of Advances in Modeling Earth Systems*,
935 12(8), e2019MS001966. Retrieved from [https://agupubs.onlinelibrary
936 .wiley.com/doi/abs/10.1029/2019MS001966](https://agupubs.onlinelibrary.wiley.com/doi/abs/10.1029/2019MS001966) (e2019MS001966
937 10.1029/2019MS001966) doi: <https://doi.org/10.1029/2019MS001966>
- 938 Weller, H., & McIntyre, W. A. (2019). Numerical solution of the conditionally
939 averaged equations for representing net mass flux due to convection. *Quar-*
940 *terly Journal of the Royal Meteorological Society*, 145(721), 1337–1353. doi:
941 10.1002/qj.3490
- 942 Yano, J. (2014). Basic convective element: Bubble or plume? a historical review.
943 *Atmos. Chem. Phys*, 14(13), 7019–7030. doi: [https://doi.org/10.5194/acp-14
944 -7019-2014](https://doi.org/10.5194/acp-14-7019-2014)